Final Report

Multi-scale experimental study of creep-fatigue failure initiation in a 709 Stainless Steel alloy using high resolution digital image correlation

NU-15-IL-UIUC-0601-01P
Project Number: 15-8432

PI: **Prof. John Lambros**
Aerospace Engineering
University of Illinois Urbana-Champaign
lambros@illinois.edu

co-PI: Prof. Huseyin Sehitoglu
Mechanical Science and Engineering
University of Illinois Urbana-Champaign
huseyin@illinois.edu

Workscope: RC-3.1
DOE TPOC: Dr. Yanli Wang
DOE Federal Manager: Dr. Sue Lesica

1. ABSTRACT

This report discusses the efforts made towards the multi-scale study of the creep-fatigue response of stainless steel 709. Multiple experimental techniques, including digital image correlation (DIC) and electron backscatter diffraction (EBSD), were used in assessing the evolution of damage accumulation during fatigue, creep-fatigue, and thermomechanical fatigue of alloy 709. The role of microstructural features, hold times, temperature, and loading profiles were quantified and the interchangeability of temperature and time was investigated. Finally, a thermomechanical fatigue model was shown to predict well the failure of samples with varying loading profiles. Results indicate that strain accumulation in 709 steel happens primarily near grain boundaries (GBs) with the strains around GBs being inversely proportional to their measured residual burgers vector. Furthermore, hot-spots for strain accumulation were shown to be the locations of eventual microcrack nucleation. The introduction of hold times to the periodic loading cycle increases the damage accumulation rate and thus shortens the fatigue life of samples–this was true for both room temperature and high temperature. Thermomechanical cycling was shown to have little effect on the end life of samples, with the damage accumulation rate for in-phase and out-of-phase cycling being similar to isothermal fatigue. The interchangeability of time and temperature was shown to be possible within the studied load, time, and temperature ranges, since deformation mechanisms driving strain accumulation did not change with temperature (up to 650°C). The Neu-Sehitoglu thermomechanical fatigue model, with constants obtained from the literature and in part from our experimental results, was applied to predict failure of isothermal creep-fatigue samples.

The main objectives of this work were to:

(a) Perform high-resolution digital image correlation measurements (HiDIC) for alloy 709;

(b) Quantify and assess damage accumulation at the microstructure under fatigue, TMF, and creep-fatigue conditions of 709;

(c) Study of the role of hold times, *i.e.*, adding a creep component, to:

Room temperature cycling,

High temperature cycling,

Failure;

(d) Study the mechanisms of thermomechanical fatigue in this alloy;

(e) Investigate the existence of a time-temperature interchangeability criterion to aid in accelerated creep-fatigue testing;

(f) Establish the validity of a combined creep-fatigue model for life prediction for 709.

This report is structured with each subsequent section detailing the efforts, results, and conclusions related to each of the objectives described, mostly in chronological order.

2. GRAIN SCALE STRAIN MEASUREMENTS

This section describes the experimental techniques used to measure strains at the microstructural level. Results from ex-situ DIC and EBSD are aligned to obtain a dataset capable of describing damage accumulation after loading.

2.1. High-resolution digital image correlation (HiDIC): Digital image correlation (DIC) is a widely used experimental technique used to obtain full-field displacement (and strain) measurements on a surface. The technique consists of correlating un-deformed and deformed images of a surface covered by a random pattern to measure the displacement field. The full-field measurements from DIC have no inherent limitations on spatial resolution; this means that image resolution is the key in obtaining the most detailed strain fields possible. In order to obtain strain fields capable of discerning non-uniformities at the grain-scale, high-resolution images of the surface are required. To reach the resolution requirements, it is necessary to place the samples under an optical microscope and take the images at high magnifications (all the results shown in this document were taken using an objective lens with 40x magnification, resulting in ~0.09 µm/pixel resolution images).

Counterbalancing the increased resolution, the disadvantages of this approach are twofold: the sample needs to be removed from the loading frame and placed under a microscope (ex-situ measurements); the field of view under a microscope is reduced (FOV of ~190x190µm using a 2000x2000 pixels camera). The first of these issues necessitates restricting the measurements to experiments with significant residual strains (inherently true for plasticity and creep), and neglecting the elastic portion of the strains. The second issue is circumvented by the use of taking multiple partially overlapping images, capable of covering the desired field of view when stitched together. This means that each contour of grain-scale strains is obtained from two sets of images that need to be stitched to form two very large images that are then correlated.

2.2. Electron backscatter diffraction (EBSD): With the strain fields in hand, the second part of the dataset required to evaluate microstructural effects on damage accumulation is obtained from electron backscatter diffraction scans. EBSD is a another widely used technique capable of providing crystal orientation maps of a sample surface. The EBSD results shown in this work were collected using a JEOL 7000F Scanning Electron Microscope (SEM) and a distance between measurement points of 1 µm. In many cases, depending on the field of view covered, it may become necessary to stitch EBSD images as well.

2.3. Alignment of HiDIC and EBSD datasets: The final, but extremely important, step of combining these two datasets (from HiDIC and EBSD) is to align the measured strain fields with the underlying microstructure. Alignment is done using five fiducial Vickers markers, at the edges of the region of interest. Even though the makers are visible in both datasets, some distortions are present in the EBSD scan results. To take this into account, a set of optical images, taken at the same magnification as the DIC images, of the etched surface of the sample prior to applying the DIC pattern, are used as an intermediate for alignment.

The following steps summarize the entire process:

1) Sample fabrication – heat treatment and machining;
2) Sample preparation – polishing down to 0.01 µm alumina solution and vibratory polishing;
3) Fiducials markers placed around the region of interest;
4) EBSD scan taken of the region of interest;
5) Surface etching using HCl solution;
6) Set of optical images of grain boundaries taken;
7) DIC pattern applied using silicon carbide particles (needed for spatial resolution and high temperature);
8) Pre-oxidation of samples for high-temperature tests;
9) Set of DIC reference images taken;
10) Sample testing – deformation;
11) Set of deformed DIC images taken.

The fiducials are used to align the DIC reference image set to the optical images of the grain boundaries; the grain boundaries themselves are used as reference points for the alignment of the EBSD data to the optical grain boundary image set. Because DIC results are automatically aligned to the reference (un-deformed) image, the strain fields can now be aligned to the EBSD data points. Figure 1 shows all the images required to perform the measurements and proper alignment. (a) Shows the results of the EBSD scan, colored by the first Euler angle. (b) shows the grain boundaries obtained by taking changes in crystal orientation >7°, these boundaries are used for the alignment of (b) and (c). (c) shows the optical image set of the etched surface, the fiducials are used to align (c) and (d). (d) shows the reference DIC image set, to which the strains field are automatically aligned during correlation.

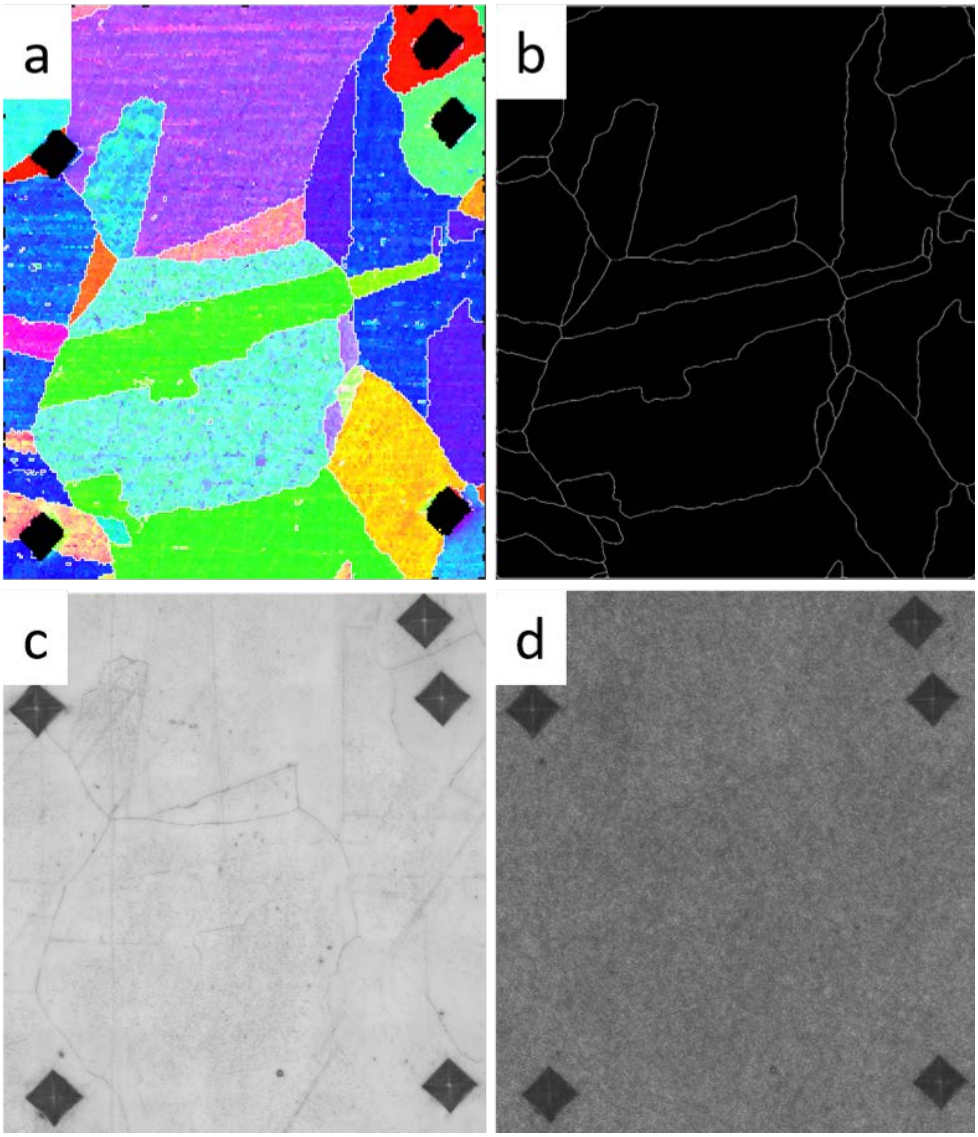

Figure 1: (a) The resulting EBSD map (painted by the first Euler angle); (b) The boundaries obtained from (a) by taking changes in orientation >7°; (c) The optical image set of the etched surface; and (d) the DIC reference image.

2.4. Experimental setup: All the tensile, creep and fatigue testing was performed using an Instron servo-hydraulic machine at the Advanced Materials Testing and Evaluation Lab (AMTEL). Figure 2 shows the entire setup, including the infrared thermometer used to measure the temperature without contact, the induction heater and its coils and the camera and lens used for in-situ DIC measurements.

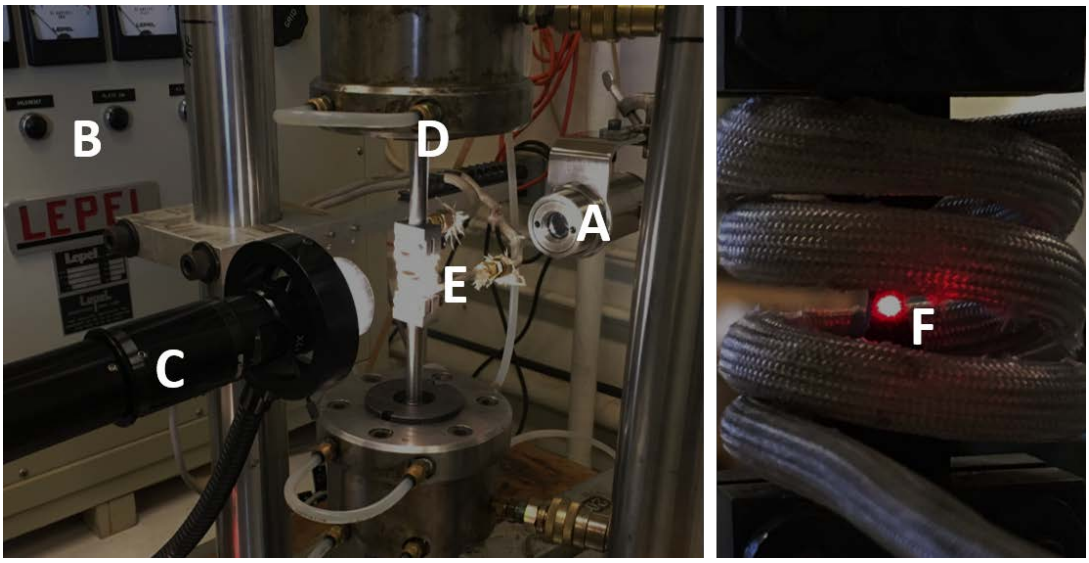

Figure 2: Load frame setup: A – Infrared thermometer; B – Induction heater; C – In-situ DIC camera and lens; D – Cooled grips; E – Induction heater coil around sample; F – Detail of sample with laser spot for IR thermometer alignment.

3. DAMAGE ACCUMULATION

To understand the mechanisms of ultimate alloy 709 material fatigue failure, the interaction between grains and the grain boundary effects must be thoroughly studied. As previously reported by many researchers, strain localization can be an indicator of crack initiation. Thus, it is essential to understand why and how strain localizes at grain boundaries in 709 steel. This section presents results of strain accumulation at the grain level at both room temperature and 650°C fatigue and relates this strain accumulation with observed microstructural characteristics.

3.1. Room temperature: Fatigue experiments were conducted at ±425 MPa at room temperature, and the fatigue life was seen to be around 2,500-3,000 cycles at this stress level. It was seen that as the specimen underwent continued cycling, residual plastic strain localized near grain boundaries. For example, in the 1,100th cycle of loading, most of the highly strained regions, denoted by red in the HiDIC results shown in Figure 3, are in the vicinity of grain boundaries. This shows the significance of grain boundaries as initiators of fatigue damage. The HiDIC strain contours overlaid with the EBSD grain boundary maps are shown for cycles 1,100, 2,100 and 3,100 in Figure 3. Also shown superposed as white

lines on the strain contours, are the microcracks seen under a microscope at each loading stage. The net residual strain for each case was 1.74%, 1.9% and 1.8% respectively

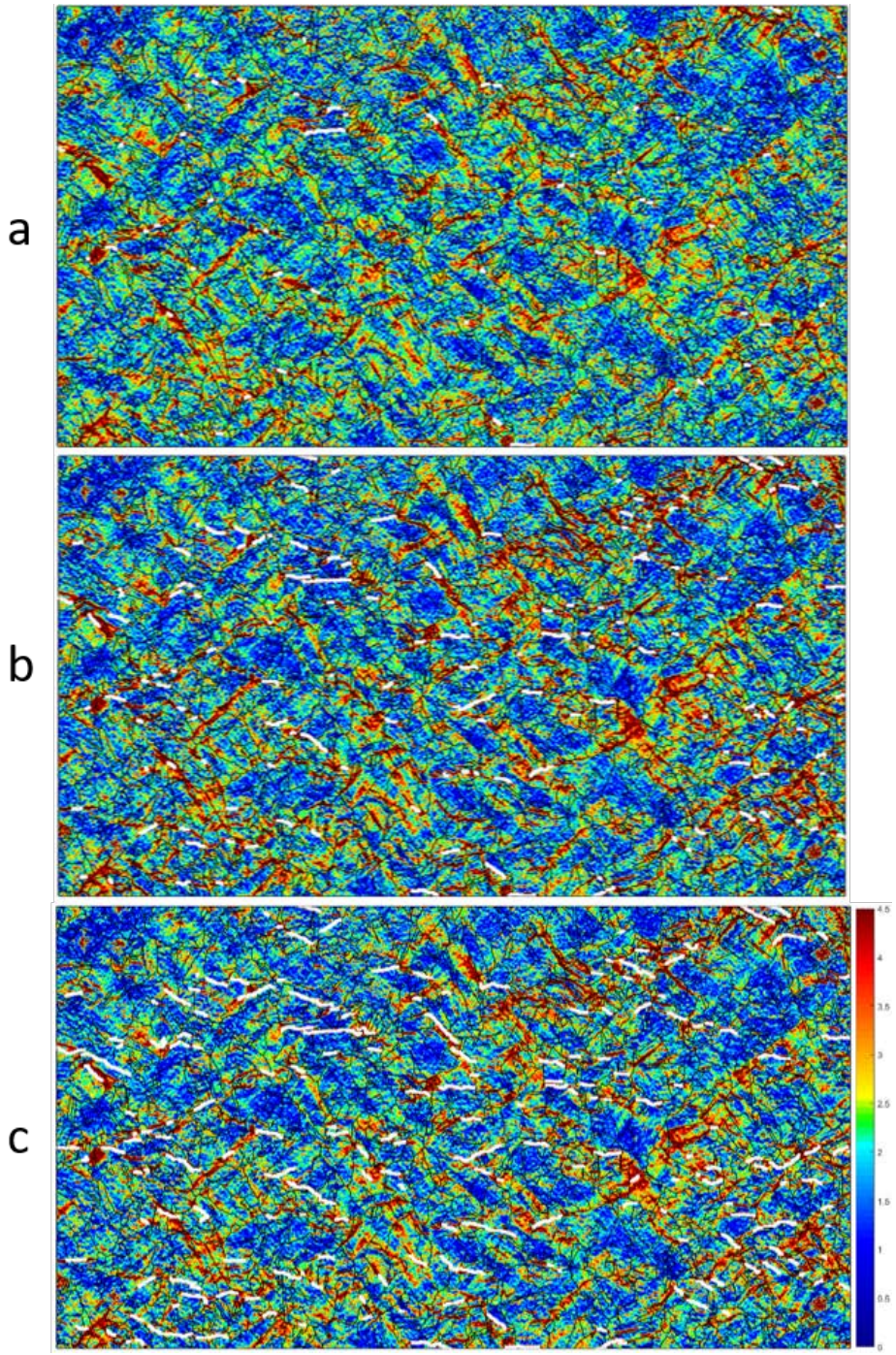

Figure 3: HiDIC measured strain accumulation in 709 during room temperature fatigue at ±425 MPa along with corresponding microcrack formation (white lines) for (a) cycle 1,100, (b) cycle 2,100 and (c) cycle 3,100.

In the room temperature experiments it was also seen that residual Burgers vector in the grain boundary plane plays a major role in slip transmission. More slip transmission across a grain boundary occurs when the magnitude of the residual Burgers vector is smaller, *i.e.*, the grain boundary forms less of an energy barrier to slip transmission. This relation is shown quantitatively from our experimental results in Figure 4 for the room temperature (RT) case (with the high temperature case discussed in the next section).

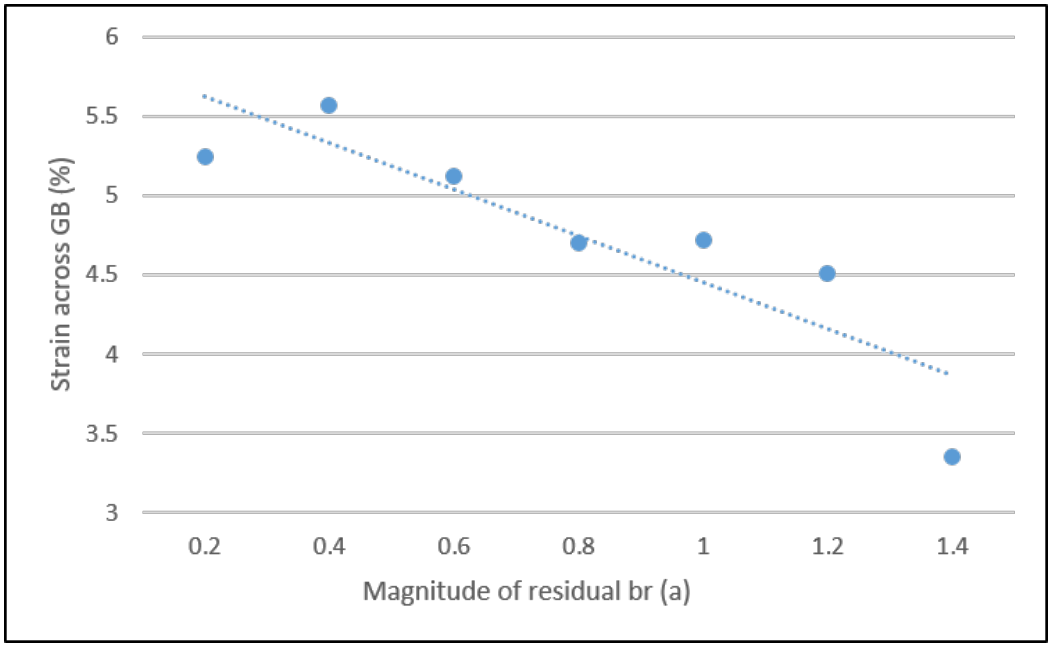

Figure 4: Total plastic strain accumulation (*i.e.*, sum of strain across both sides of boundary) *vs*. residual Burgers vector across all grain boundaries in ROI for RT fatigue sample.

3.2. High temperature: A similar set of experiments was conducted to assess the microstructural damage content and its relation to the microstructure at 650°C. It was seen that there was considerable variability in the fatigue life observed in experiments with stress amplitude ±230 MPa, with the strain range being the actual driving force behind damage. For these conditions, some samples showed a continuous increase in strain range while others reached a steady-state plastic hysteresis stress-strain loop.

Additionally to these observations of fatigue life variability and failure mode variability, we want to ultimately link these to microstructural stain accumulation measured by the HiDIC technique. Figure 5 shows HiDIC strain maps overlaid with the grain boundary locations illustrating the strain accumulation/transmission near the grain boundaries occurring at 650°C fatigue loading. The image on the left is after the very 1st cycle of deformation at ±230 MPa and 650°C, with a mean residual axial strain

of 0.8% already accumulating, and the image on the right is after the 100th cycle of deformation with a mean residual axial strain of 1.4%.

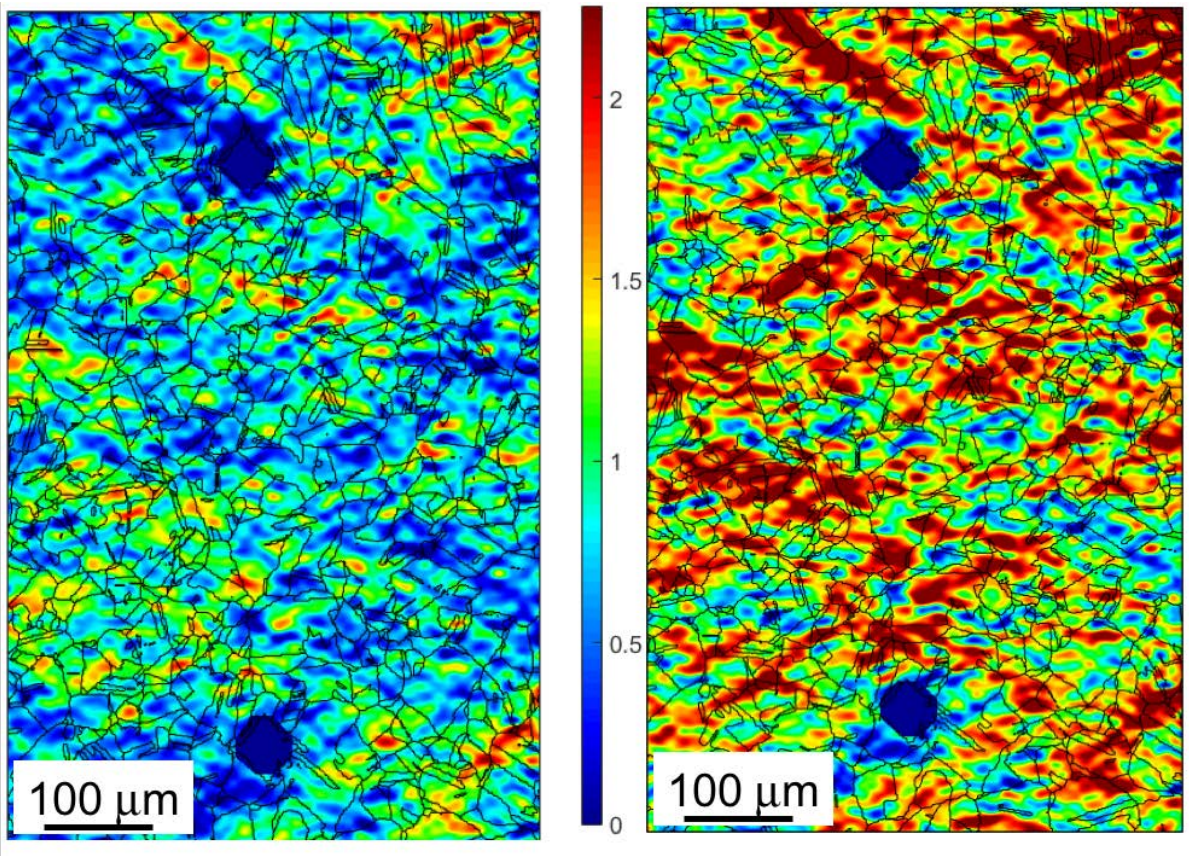

Figure 5: DIC strain map overlaid with EBSD grain boundaries for 650°C elevated temperature fatigue tests. Cycle 1 is shown on the left and cycle 100 on the right. The solid blue circles in the middle are Vickers indentation marks.

As mentioned for RT above, residual Burgers vector across a grain boundary plane plays a major role in slip transmission. More slip transmission across the grain boundary occurs if a lesser magnitude of the residual Burgers vector is left behind after transmission. Figure 6 shows the slip-residual Burgers vector plot, analogous to the one in Figure 4, for the case of 650 °C. The linear trend seems to be maintained at high temperature and consequently the magnitude of residual Burgers vector can be used to indicate a precursor to crack formation in this case as well.

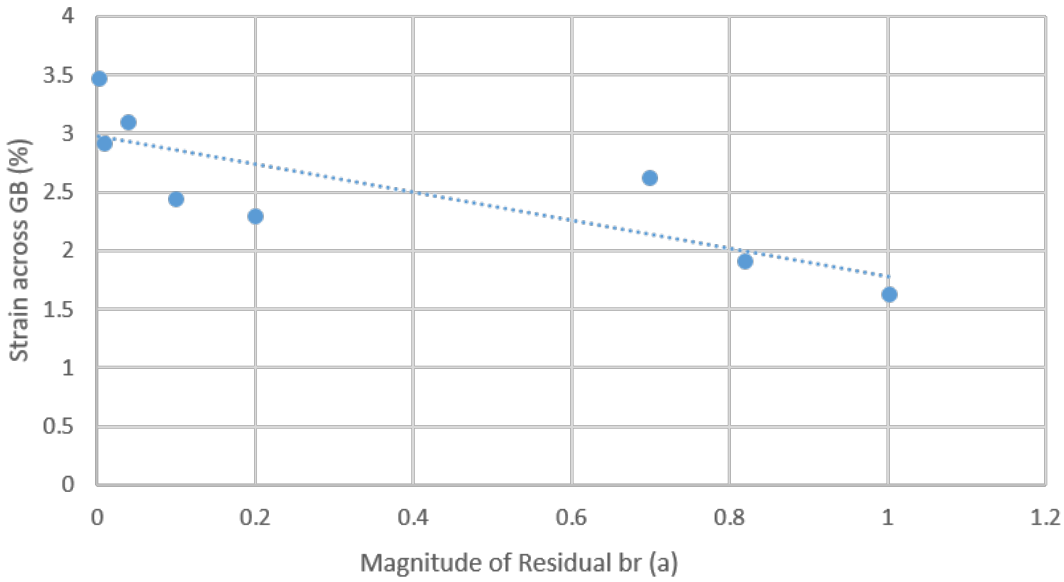

Figure 6: Total plastic strain accumulation (i.e., sum of strain across both sides of boundary) vs. residual Burgers vector across all grain boundaries in ROI for 650°C fatigue sample.

3.3. Conclusions: Experiments show that strains accumulate primarily near grain boundaries both at room temperature and 650°C. For RT, microcracks were observed to nucleate at locations where strains accumulate from early cycles, while at high temperature, a high variability of fatigue life, caused by differing modes of failure was observed. For samples with longer lives, the same microcracking behavior, as in RT, was observed at 650°C, but for the samples with lower lives, which presented ratcheting, a dominant crack was shown to form from the edge. For both cases, strain accumulation was then shown to correlate well with the magnitude of residual Burgers vector, which can be used as a factor to decide the onset of fatigue crack initiation.

4. ROLE OF HOLD TIMES – ROOM TEMPERATURE

In this section, the role of hold periods on fatigue life of stainless steel 709 specimens is described both at the macroscale (*i.e.*, sample scale) and at the microscale (*i.e.*, grain scale). 709 steel does present viscoplastic behavior even at room temperature, as also does stainless steel 316 (the most common austenitic stainless steel with similar composition to 709). With this in mind, the decision was made to study the 709 material's creep-fatigue behavior at room temperature, as well as, at higher temperatures.

Time effects and strain hardening in metals are necessarily related to irreversible inelastic strain [1]. Since metals rarely present any viscoelastic behavior, it is very hard to study time-dependent behavior, such as creep, in isolation from the material's plastic deformation behavior. Various authors have previously reported the accumulation of plastic strain during hold times for austenitic stainless steels, such as 316 and 304 [2, 3]. Both these studies concluded that time-dependent constitutive equations are required to accurately describe the behavior of these steels at room temperature. Separating the creep and fatigue responses of materials that exhibit this type of behavior is an arduous task. Not many studies have been reported on room temperature creep-fatigue [2], but a multitude of such studies can be found for high temperature applications of TiAl and Nickel super-alloys for example [4,5]. All these studies showed that fatigue life decreases with an increase in hold times.

The first step taken in order to determine the macroscopic behavior of stainless steel 709 under creep-fatigue loading conditions was the study of room temperature plastic creep. To activate creep phenomena at shorts time scales we first loaded the material to a significant level of plastic strain (50% above the yield stress) and then held the load constant at that level. The result will represent a measure of plastic creep of the material. Figure 7 shows the residual strain accumulated by five samples loaded at 500MPa for different lengths of time. It is clear that there is a diminishing effect with longer hold times where the creep strain does not increase beyond a certain hold time, as has also been reported by other authors [5].

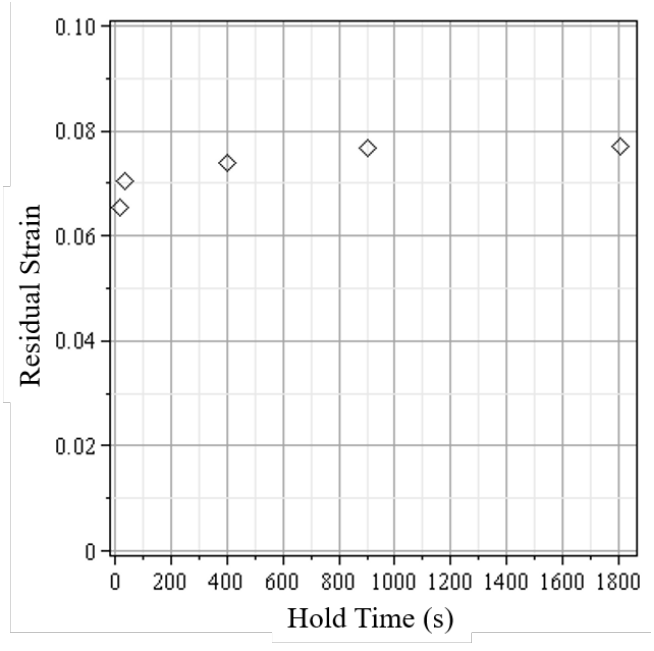

Figure 7: Residual plastic strain after plastic creep at different hold times.

Proceeding to the study of the macroscopic response of 709 under combined creep and fatigue conditions, a sample was loaded cyclically from 0 to 500 MPa, at a stress rate of 2.5 MPa/s and held at the maximum load for 15 minutes (900 s) during each cycle. Figure 8, which plots the creep stain accumulation as a function of cycle, clearly shows that the accumulated strain decreases for each cycle, and also shows that after the 12th cycle the strain accumulation reaches a steady-state. This particular experiment was conducted until the 64th cycle and the strain never stopped to accumulate at a near constant base-rate, although it had reached a steady state. This ratcheting-like behavior has been previously reported for 304L stainless steel [3].

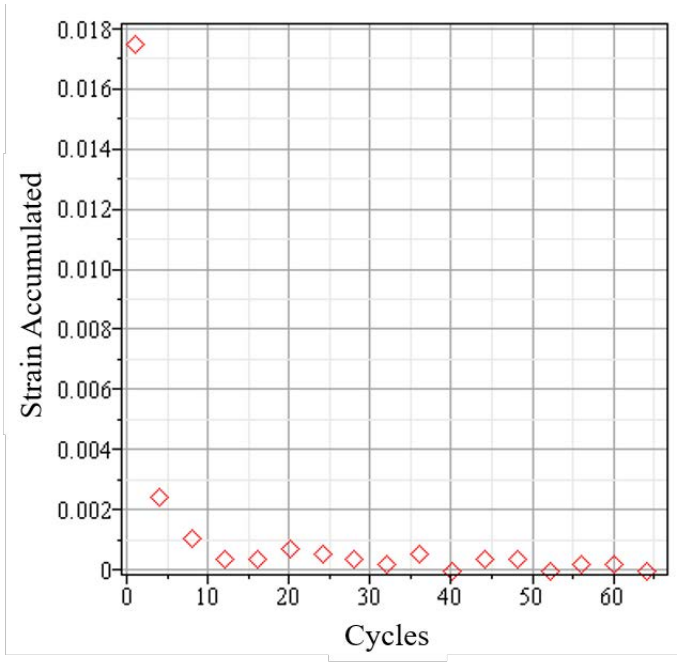

Figure 8: Strain accumulated during hold for each measured cycle for plastic creep-fatigue with 15 min hold time.

In order to explore the microscale behavior during RT creep-fatigue of stainless steel 709, a series of experiments were conducted using the ex-situ HiDIC technique describe earlier. A spatial resolution of 0.107 pixels/µm was used to visualize the deformed sample after loading and produce high-resolution residual plastic strain measurements. To somewhat isolate the effects of plasticity and creep, a sample was loaded in two steps. First, it was loaded up to 500MPa and unloaded right after reaching maximum load, then it was loaded again to 500MPa and held for 30 minutes. After each step a series of HiDIC images was taken, so the accumulated strains due to plasticity and creep could be separately measured. Figure 9 shows the resulting residual strain fields after each one of these loading steps.

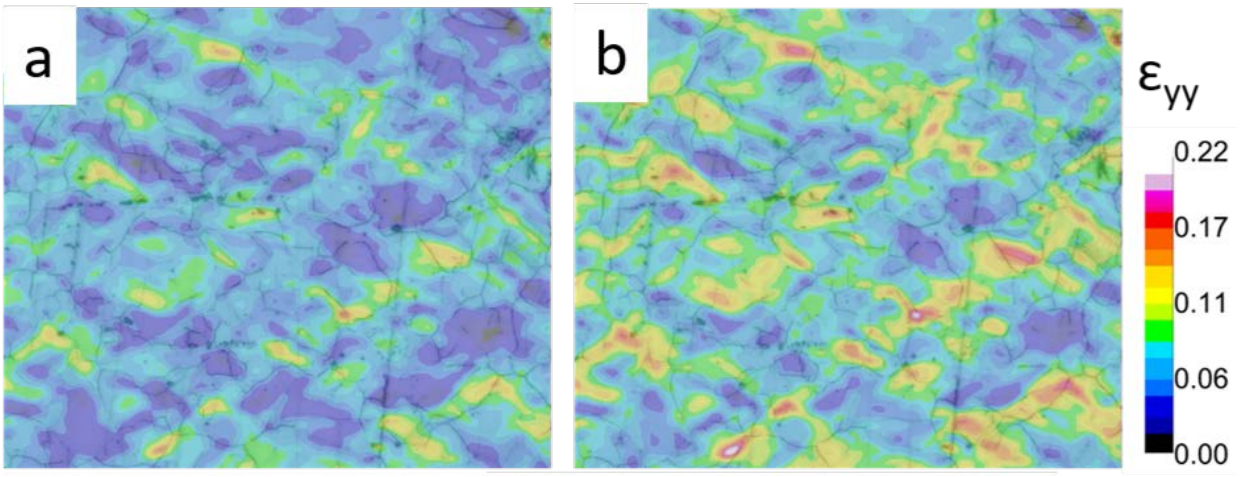

Figure 9: (a) Residual axial strains after a tensile cycle (500 MPa) without any hold time; (b) Residual axial strains in the same sample after a subsequent hold time of 1800 s (again at 500 MPa).

These contours show that strain accumulates at specific locations whether through plastic or creep deformation. Because the shape of the strain fields is very similar, it implies that creep straining occurs at the *same locations* where plastic strains had initially developed.

Finally, the results of a fully reversed creep-fatigue experiment are shown. Here, a sample was loaded to 500 MPa and held there for 30 s, being subsequently loaded to -500 MPa and again held there for 30 s. For each half-cycle of loading, the sample was removed from the loading frame and a set of images was taken. Figure 10 shows the residual DIC-measured strain fields for all loading points were DIC data were collected ranging from cycle 1 to 8 either at the tensile peak or the compressive peak of the cycle, as indicated by "T" or "C". It is useful to see the evolution of the strains as a sequence and especially note the fact that they tend to accumulate always on the same spots. In addition to the contours in Figure 10, Figure 11 shows the measured average residual strains which exhibit a quick decrease in strain (*i.e.*, recovery) after the initial cycles followed by a gradual increase.

An intriguing aspect of the results is the fact that the residual strains never reach any negative values, even after 30 s hold at -500MPa. This can be interpreted as a high degree of irreversibility of the strains accumulated during the tensile hold period leading to an asymmetry in the hold period effect that needs further exploration. However, a likely explanation can probably be found in the fact that it is known that slip is generally bi-directional (same in tension and compression) in fcc metals. In contrast, in creep, tension-compression asymmetry has been observed in fcc metals. The exact mechanisms of creep are not clear in our case, but there appears to be significant tension-compression asymmetry likely controlled by a hydrostatic stress effect.

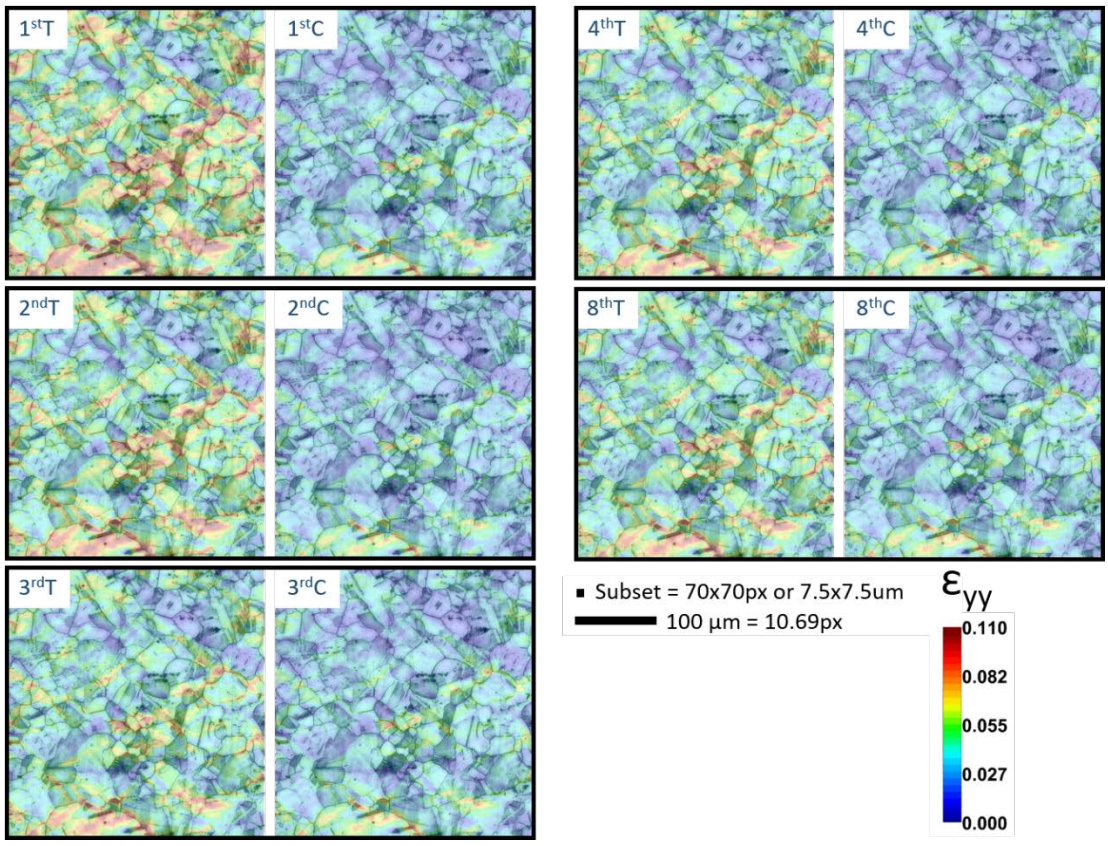

Figure 10: DIC-measured residual plastic strain fields for all 10 loading points were images were collected. Measurements at cycles ranging from 1 to 8 either at the tensile or compressive peaks, as indicated by "T" or "C".

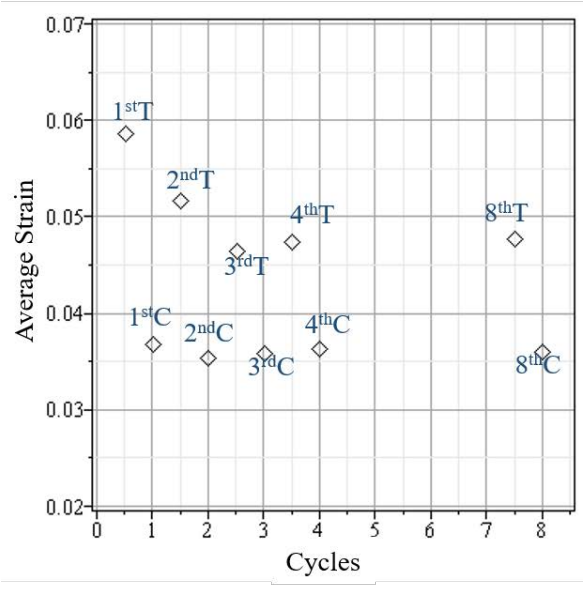

Figure 11: Average strain for each DIC measurement state as denoted for each cycle.

Conclusions: The conclusions drawn from this part of the study on the role of hold times on the room temperature fatigue life of stainless steel 709 are summarized as follows:

1) Stainless steel 709 presents highly viscoplastic behavior even at room temperature;
2) Somewhere around 60s hold time, the plastic creep strain reaches a limiting value;
3) Repeated hold cycles produce diminishing strain accumulation, although strain never stops accumulating with cycling;
4) Strains accumulate at the microstructure in preferential locations, namely grain boundaries, even from very early loading cycles, and for both the plastic and creep aspects of the deformation;
5) Subsequent cycles cause strain accumulation at the same locations where it first occurred, regardless of creep or fatigue accumulation;
6) Compressive holds are not able to recover the strains accumulated during tensile holds.

5. ROLE OF HOLD TIMES – HIGH TEMPERATURE

This section, following the outline of the previous, describes the role of hold periods on fatigue life of stainless steel 709 at high temperature (650°C). Before proceeding to creep-fatigue loading conditions, the high temperature (650°C) behavior of stainless steel 709 purely under plastic creep conditions was studied first. In order to activate and accelerate creep phenomena for the short time scales possible in our laboratory setting, the material was loaded to a stress level of 50% above the yield stress (of each applicable temperature, either room or elevated temperature) and then held at that load for various periods of time.

In order to normalize the results to allow comparison between RT and 650°C, we will employ the concept of *specific creep strain*, introduced in prior creep studies, as creep strain per unit stress [6-7]. However, since we do not have a uniform strain sample–it is an hourglass geometry–we will introduce the concept of *specific creep displacement* where the creep displacements are divided by the maximum stress applied in each case. To explore the early stages of creep strain development which is perhaps more relevant in the creep-fatigue experiments to follow, a series of 5 short-hold creep experiments were performed at both RT and 650°C, with the samples being held at 500 MPa and 250 MPa, respectively, for 15 s, 30s , 150 s, 300 s and 900 s. The resulting accumulated specific displacements are plotted against hold time in Figure 12.

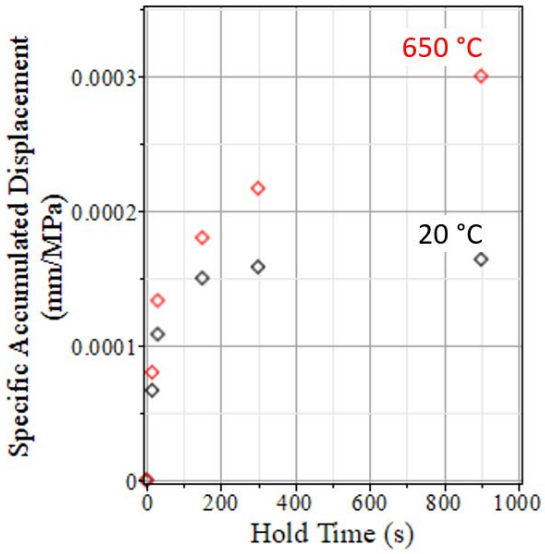

Figure 12: Specific accumulated displacement vs. hold time for 10 different samples held at either 500 MPa (RT) or 250 MPa (650°C).

Proceeding to the study of the macroscopic response of 709 under combined creep and fatigue at high temperature, a sample was loaded cyclically from 0 to 250 MPa at a stress rate of 2.5 MPa/s, while being held at the maximum stress for 60 s at each cycle. Figure 13 shows the plot of accumulated displacement as a function of cycle number. The displacement stopped accumulating, with the sample essentially reaching fully elastic response at around 6 cycles, *i.e.*, a shakedown behavior.

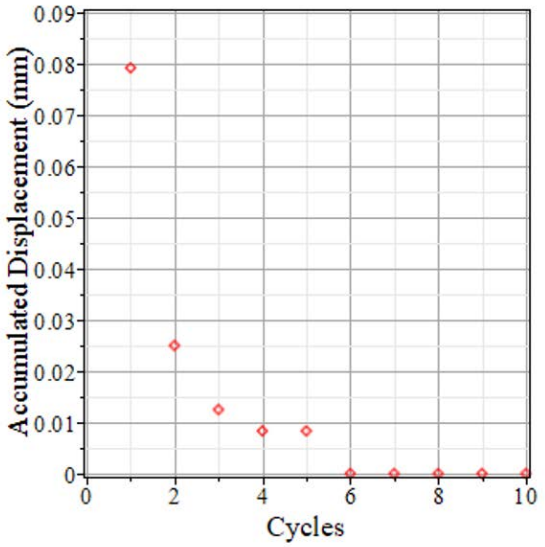

Figure 13: Accumulated displacement vs cycle number.

Finally, microscale strain results for a fully reversed creep-fatigue experiment at 650°C are shown in Figure 14. As was observed for room temperature, strains accumulate at preferential locations, creating a non-uniform strain field that retains it localization for the entire duration of loading. From as early as the first cycle, the strain field assumes a spatially localized distribution that remains practically unchanged for the remaining cycles, varying only in the magnitude of the strain values that are added or subtracted depending whether the images are taken after a compressive or a tensile half cycle. Additionally, the strain fields reach a steady-state after the first cycle, that is, the residual strains present on the 3rd cycle are the same as those present on the 2nd cycle.

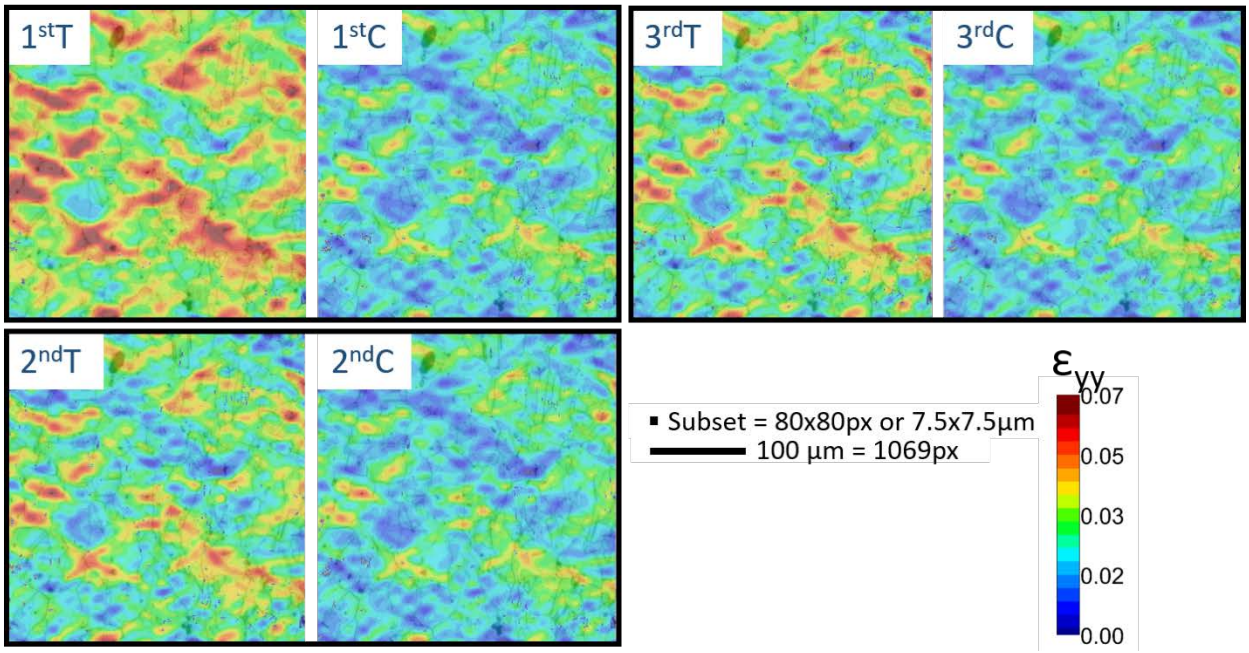

Figure 14: DIC-measured residual plastic strain fields for all 6 loading points where images were collected. Measurements at cycles 1 to 3 either at the tensile or compressive peaks, as indicated by "T" or "C".

Figure 15 shows a plot of the average microscale residual strain at each data point, making this observation more obvious. Such a strain recovery behavior was also observed at room temperature, though at elevated temperature the strain recovery happens faster (in fewer cycles).

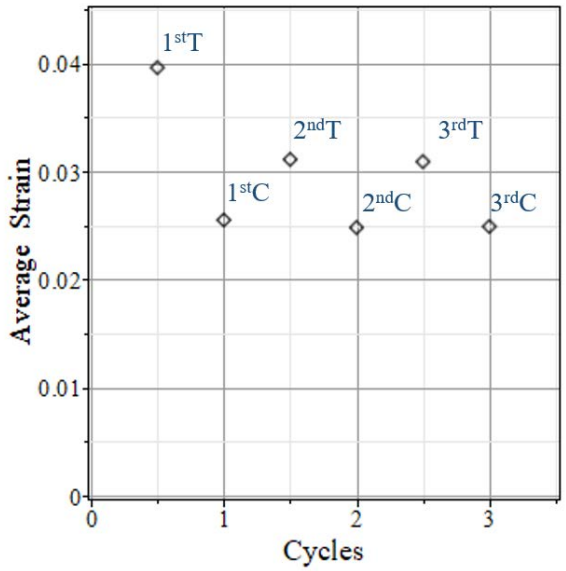

Figure 15: Average strain for each DIC measurement state as denoted for each cycle.

Conclusions: The conclusions drawn from this part of our study on the role of hold times on the high temperature fatigue of stainless steel 709 can be summarized as follows:

1) Stainless steel alloy 709 presents even higher viscoplastic behavior at high temperatures than at room temperature;

2) Repeated hold cycles produce diminishing strain accumulation;

3) Strains accumulate at the microstructure in preferential grain boundary locations, even from the first loading cycle, for both the plastic and creep aspects of the deformation;

4) Subsequent cycles cause strain accumulation at the same locations where it first occurred, regardless of creep or fatigue strain accumulation;

5) High degree of irreversibility of the strains meaning that the residual strain-state never crosses zero after the first loading half cycle.

6. ROLE OF HOLD TIMES – FAILURE

This section summarizes the effects of hold times on the failure of creep-fatigue samples both at room temperature and high temperature. Overall, it is expected that hold times act to decrease fatigue lives of samples. In order to verify this, an SN curve was constructed from a series of samples loaded cyclically until failure. Figure 16 shows the SN curve for samples loaded both at room temperature and at 650°C, with different hold times.

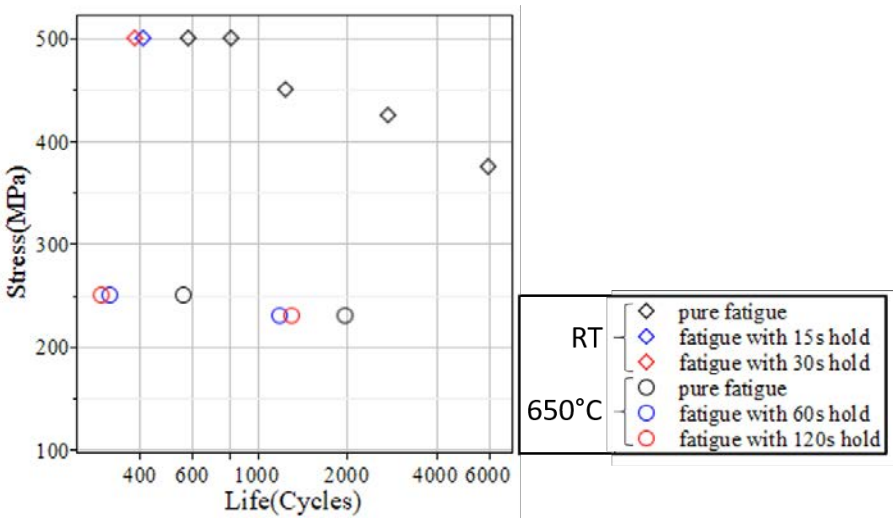

Figure 16: Stress-life curve comparing pure fatigue and creep-fatigue tests at RT and at 650°C.

Although more experiments would be required to establish a complete database on the effect of temperate and hold times, the results consistently show that hold times have a negative effect on life, as was expected and reported by other authors [8-10]. The only "unexpected" result comes from the fatigue with hold time experiment at 650°C under 230 MPa maximum stress, where the specimen with longer hold time had a longer life, but this difference is within the fatigue life variability.

The effect of hold times on the development of microcracks was also studied, with results showing that microcracks still develop at locations where strains are accumulated from very early on. Figure 17 shows the stitched DIC image obtained after 400 cycles for a sample loaded at room temperature with stress amplitude of 500 MPa and hold times of 30 s, as well as the contour plots for the residual axial strains obtained after the initial 100 of those cycles. The arrows on the images point to the locations where cracks were observed (through optical microscopy) to be present after the 400th cycle.

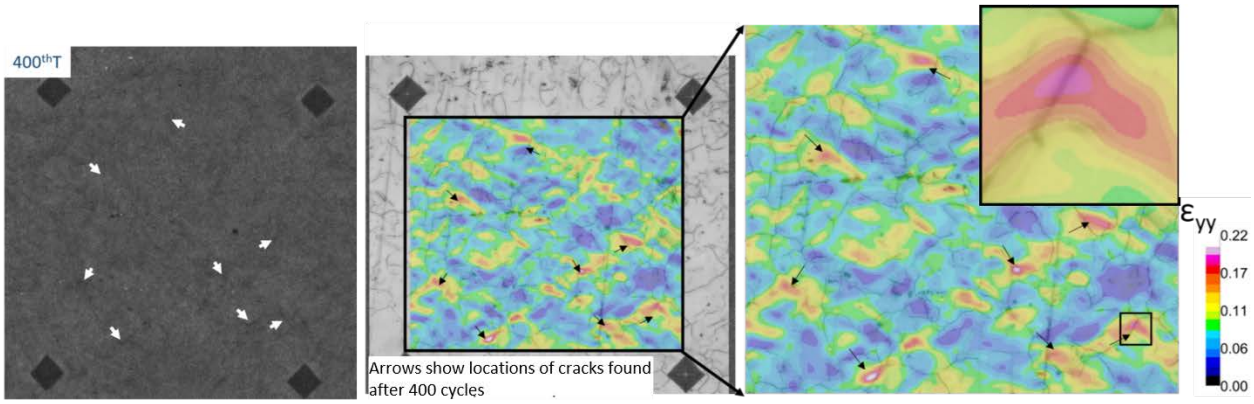

Figure 17: Overlaid contour plots of residual axial strain obtained after 100 creep-fatigue cycles with arrows indicating locations where cracks were found after 400 cycles.

7. THERMOMECHANICAL FATIGUE

Previous sections explored the behavior of stainless steel 709 under isothermal fatigue, with temperature kept constant at either room temperature or 650°C. This section presents the results of our study on the behavior of the material under conditions more compatible with the start-up/shut-off cycling that is observed during operation. Thermomechanical fatigue can be defined as the situation where both loading and temperature vary with time, either in-phase or out-of-phase.

Stress control and strain control experiments were conducted on hourglass shaped samples in a servo-hydraulic load frame. Temperature was cycled between 350°C and 650°C. Stress control experiments were performed with a stress range of ±260 MPa. As reported earlier in a previous report, stress control isothermal experiments conducted at 650°C resulted in high variability of fatigue life. Moreover, stress control TMF experiments also involved significant ratchetting of the sample which is generally undesirable and an off-design condition. To mitigate this ratchetting issue, strain control experiments were performed. Figure 18 shows a typical result of the strain vs. temperature curve for an in-phase experiment, demonstrating that strain control produces a stable strain range over a wide range of test cycles.

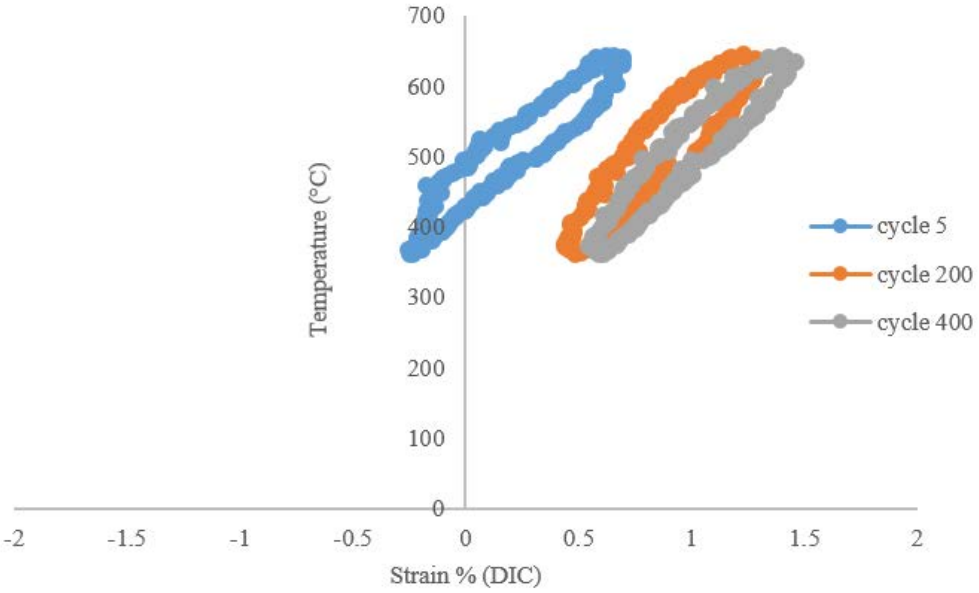

Figure 18: Strain-temperature history for in-phase experiment.

Figures 19, 20 and 21 present stress vs. strain loops for measured cycles for in-phase, out-of-phase and isothermal strain-controlled fatigue tests. Figure19a shows the loops for an in-phase test with

compressive mean stress while Figure 19 b shows the same, but for a tensile means stress. Figures 20a and b have different nominal strain ranges.

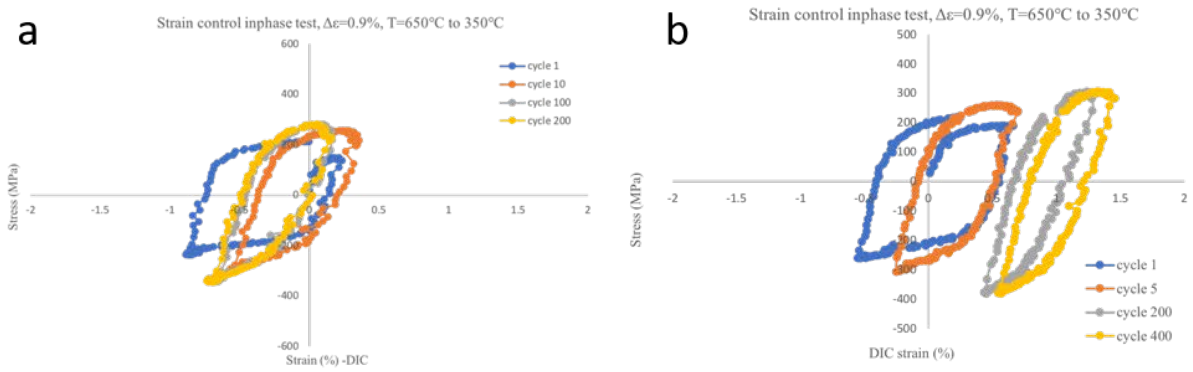

Figure 19: Stress-strain loops during strain control in-phase TMF with (a) compressive mean stress, (b) tensile mean stress.

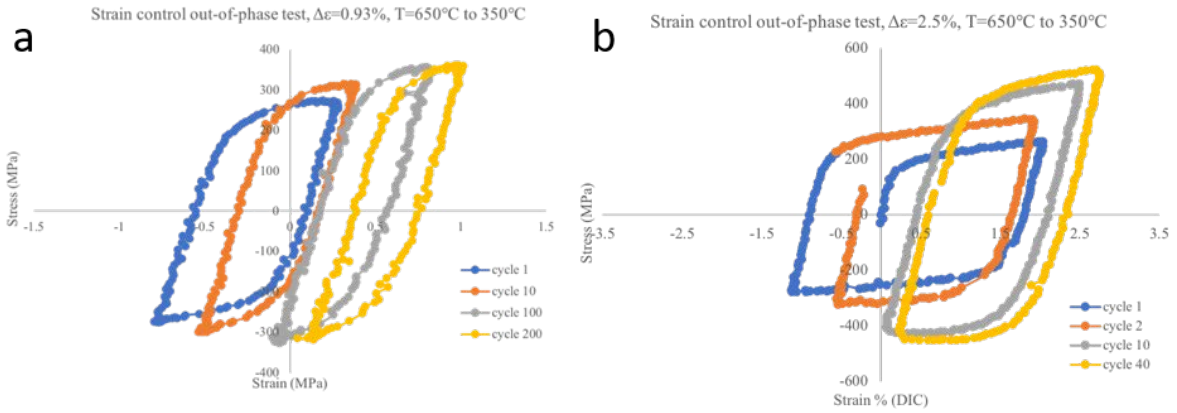

Figure 20: Stress-strain loops during strain control out-of-phase TMF with strain range (a) 0.93%, (b) 2.5%.

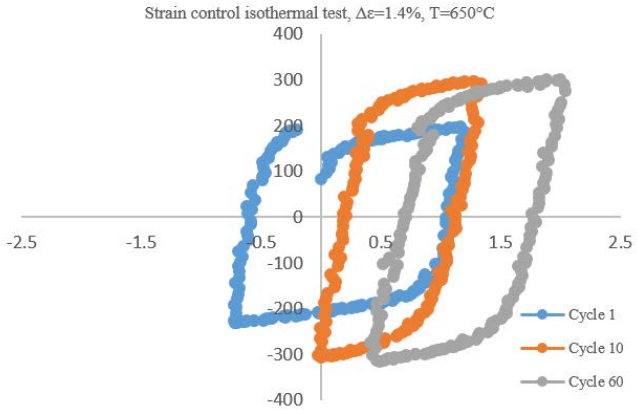

Figure 21: Stress-strain loops for isothermal experiment with a strain range of 1.4%.

The fatigue lives of all tested samples (stress or strain control, isothermal or TMF) were plotted against the strain range at half-life to obtain a "universal" strain-life curve as shown in Figure 22. We can see from this curve that the fatigue lives of the isothermally cycled samples and of the TMF samples follow the same trend. Cycling the temperature does not immediately appear to have an added detrimental effect on fatigue life. Furthermore, we can see that the fatigue lives of these samples are generally dictated by their strain range rather than maximum stress.

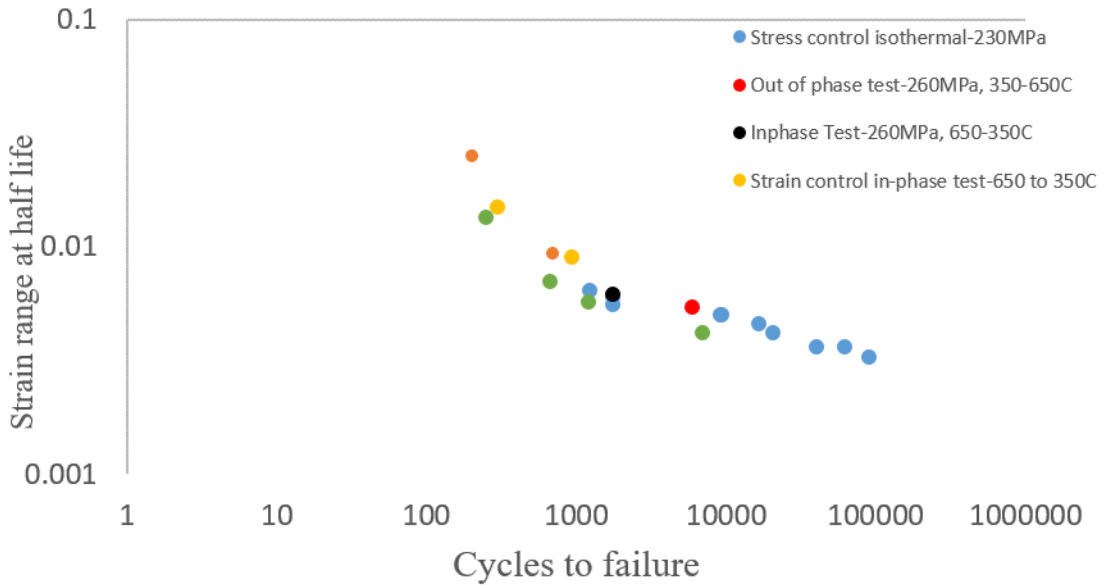

Figure 22: Strain vs. life plot for all experiments conducted in this part of the study.

To further understand what drives the fatigue lives of the samples subjected to isothermal and thermomechanical fatigue, surface and edge cracks formed in the samples were investigated under optical and electron microscopy. Energy dispersive spectroscopy (EDS) of the samples cycled isothermally and under TMF reveal oxide intrusion in both the cases, as indicated by the different contrast in the SEM images of Figures 23a and b, and confirmed by the EDS spectral map shown Figure 24.

EBSD was also done to extract grain orientation information around the cracks, Figures 25a,b and c. We can see that the edge cracks always start out as intergranular in nature and become transgranular when the crack reaches a length of about 60-70 μm. From the EBSD maps we can also see that the damage mechanism is the same for in-phase, out-of-phase, and isothermal fatigue. The cracks are mixed mode in nature and exhibit both intergranular and transgranular characteristics in both cases.

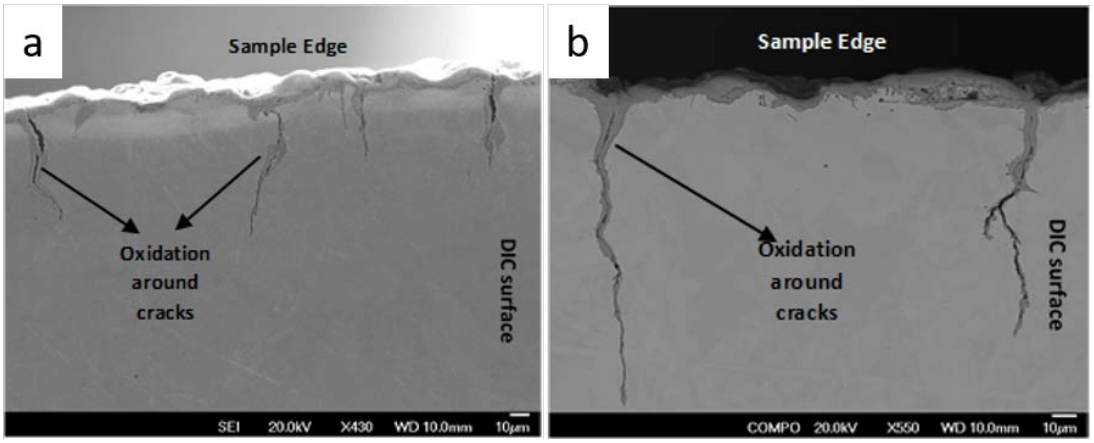

Figure 23: Oxide intrusions around cracks in (a) TMF sample, (b) isothermal fatigue sample.

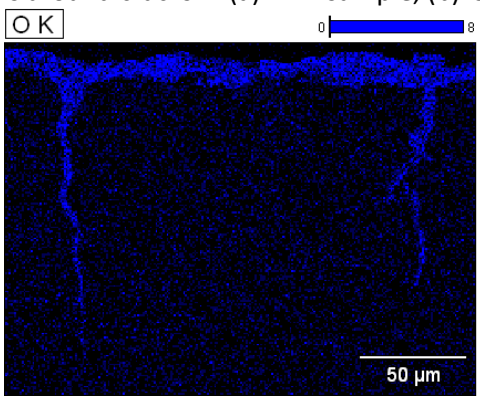

Figure 24: EDS spectral map confirming oxygen concentration around cracks in isothermal fatigue.

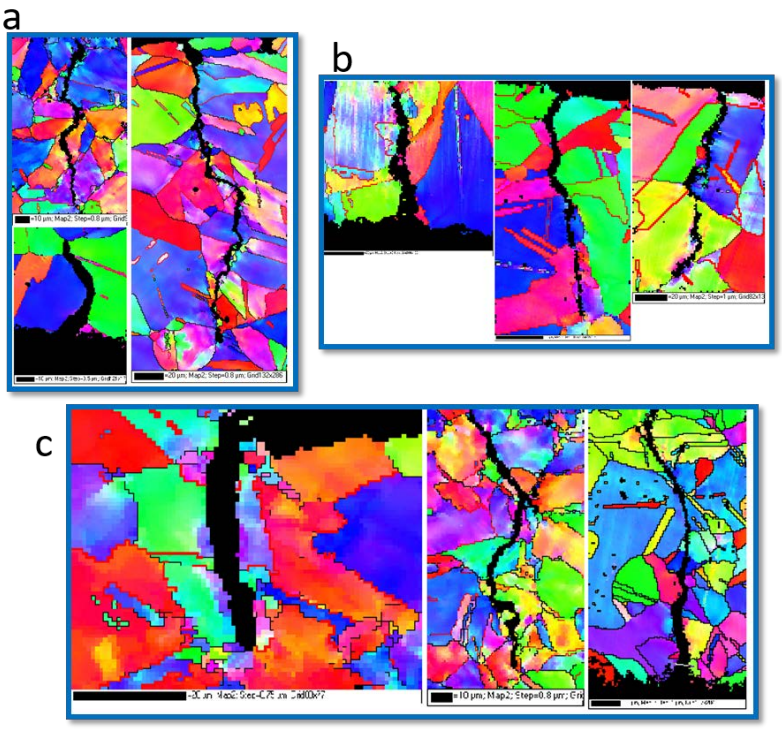

Figure 25: Cracks in (a) In-phase TMF; (b) isothermal fatigue and (c) out-of-phase TMF.

Conclusions: The conclusions drawn from this part of our study on the differences and commonalities of thermomechanical fatigue (in-phase and out-of-phase) and isothermal fatigue are:

1) Cycling the temperature along with the stress/strain does not seem to affect the fatigue life of alloy 709;

2) The life of the sample at high temperatures is dictated by its strain range rather than the peak stress;

3) Oxide intrusions along the crack faces accelerate the crack growth at high temperatures. These intrusions were found both in isothermal and TMF samples;

4) Edge cracks always initiate at grain boundaries and become transgranular as the crack exceeds 65 μm in length.

8. TIME-TEMPERATURE INTERCHANGEABILITY

Time–temperature relationships can be useful in reducing experimental testing times since by increasing the temperature at which a creep experiment is conducted the amount of time required to reach failure is reduced. Time–temperature parameters, such as Larson-Miller's, can then be used to predict the failure times for lower temperatures. This practice, although very useful, needs to be applied with care. Since the underlying mechanisms that govern damage accumulation in creep are a function of temperature [11], the equivalence between high temperature–short duration tests and low temperature–long duration tests should take damage mechanisms into account, especially when the goal is to develop mechanics-based models for predicting failure.

In addition, it has been increasingly accepted that microstructural effects are largely responsible for controlling the mechanisms of deformation and strain accumulation during creep loading [12, 13]. This is yet another source of possible error in the immediate application of time–temperature parameters while disregarding the underlying behavior of the material. Because of this, it is necessary to investigate how the mechanisms of damage accumulation at the microscale vary with both temperature and time. This section outlines such an investigation about the time–temperature relationship of damage (measured as residual strain accumulation) during creep loading of stainless steel 709 and its governing mechanisms.

Creep experiments were conducted on stainless steel 709 samples at two different temperatures (300°C and 500 °C) at the same stress value (250 MPa), with varying hold times. The specific protocols of the tests conducted, which included two loading steps, are summarized in Table 1.

Table 1: List of experiments conducted on each of 5 stainless steel 709 samples.

Sample #	Stress (MPa)	First loading step (Temp. - Time)	Second loading step (Temp. - Time)
1	250	300 °C - 60 min	500 °C - 5 min
2	250	500 °C - 5 min	300 °C - 60 min
3	250	300 °C - 120 min	500 °C - 10 min
4	250	500 °C - 0 min	500 °C - 5 min
5	250	500 °C - 0 min	500 °C - 10 min

The same procedure described in previous sections was used here to obtain HiDIC residual strain fields for each sample after each loading step. Figures 26 and 27 show the residual strain fields obtained for samples 1 and 2 after each loading step.

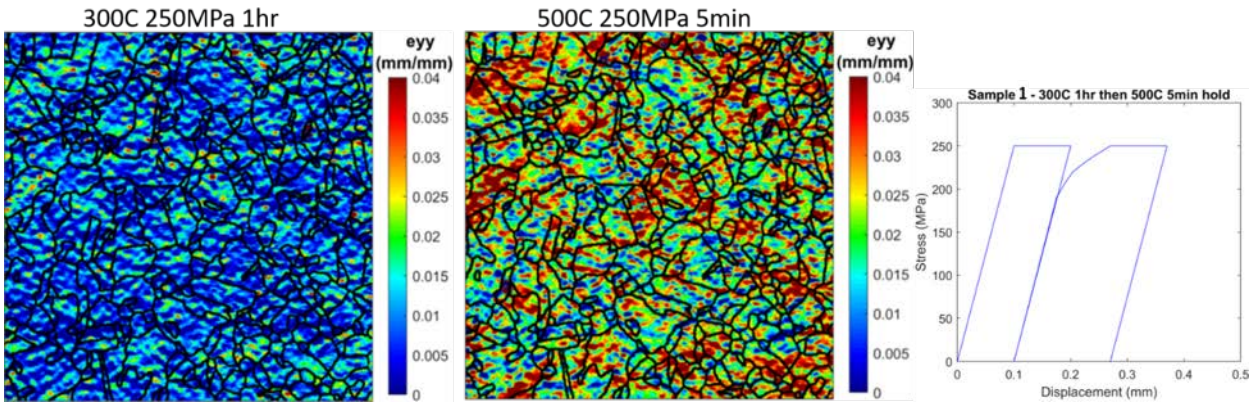

Figure 26: Residual axial strain field obtained for sample #1 at the end of the first (left) and second (middle) loading cycle, and schematic of corresponding stress vs. displacement curve (right).

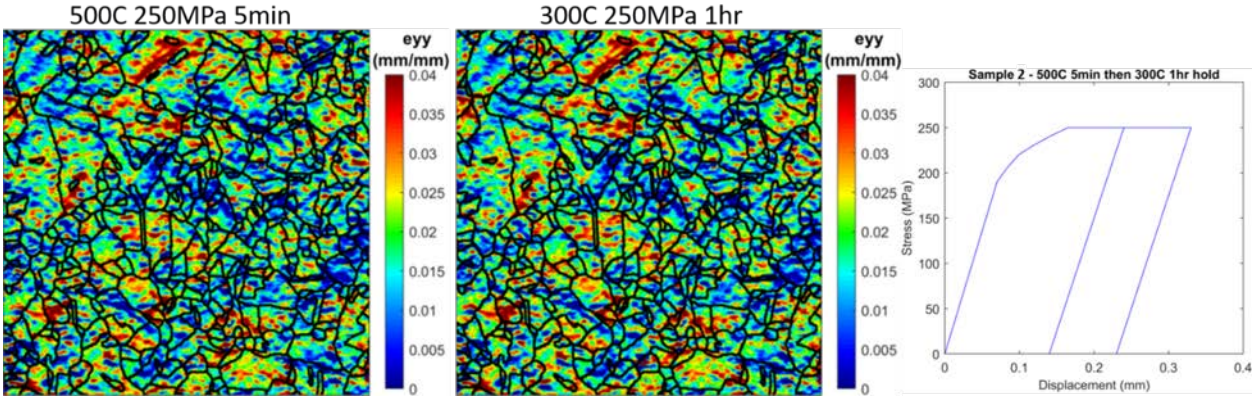

Figure 27: Residual axial strain field obtained for sample #2 at the end of the first (left) and second (middle) loading cycle, and schematic of corresponding stress vs. displacement curve (right).

From sample #1, we observe that the damage resulting from 5 minutes under 500°C was far greater than over 1 hour under 300°C. However, we should observe that under 250 MPa the sample will undergo plastic deformation at 500°C, while under 300°C it remains elastic. These two regimes of deformation are therefore, from here onward, designated as elastic creep and plastic creep. Sample #2 was subjected to the reverse of the loading steps of sample 1, *i.e*. the 5-min hold at 500°C was followed by a 1-hr hold at 300°C. The resulting strain fields show that the hardening caused by the first step, made the second step less damaging. The average strains for the first and second steps were 0.0239 and 0.0241, a negligible 0.02% difference, much lower than the average strain after the first step of sample #1, 0.0081 (or 0.8%). Sample #3 was subjected to the same loading steps as sample #1, but had the stresses held for twice as long in each cycle. By doubling the length of the experiment from 1 hour at 300° followed by 5 minutes under 500°C to 2 hours and 10 minutes respectively, the total amount of average strain accumulated increased by 0.003 (or 0.3%). Additionally, half (0.15%) of that increase came from the elastic creep portion while the other half came from the plastic creep portion. This result would suggest that an hour at 300°C is equivalent to 5 minutes under 500°C, but this result might not be correct, since the pure plasticity part of the strains are not being accounted for in the HiDIC results which by their ex-situ nature involve only residual plastic strain.

To circumvent this issue, sample #4 was loaded at 500° up to 250 MPa, but as soon as the maximum load was reached the sample was unloaded and a set of images was taken. Then, the sample was reloaded up to 250 MPa and held for 5 minutes. The same steps were taken for sample #5, but with a double (10 minutes) hold time instead. The results from these two experiments are shown below, Figure 28, in a bar plot, along with the result from the first load cycle of sample 1. The idea behind this plot is to separate the effects of plasticity, plastic creep, and elastic creep. The 1-hour elastic creep at 300°C from the first sample accumulated almost exactly the same amount of average strain as that of the 10-minutes elastic creep from sample #5. By isolating the plasticity and creep parts of the load, the conclusion is different than what could be perceived from the tests that contained all the strains in a single step. Furthermore, Figure 28 also shows that by doubling the amount of time at maximum load from 5 minutes to 10 minutes, the average strain accumulated during that period went from 0.43% to 0.79%

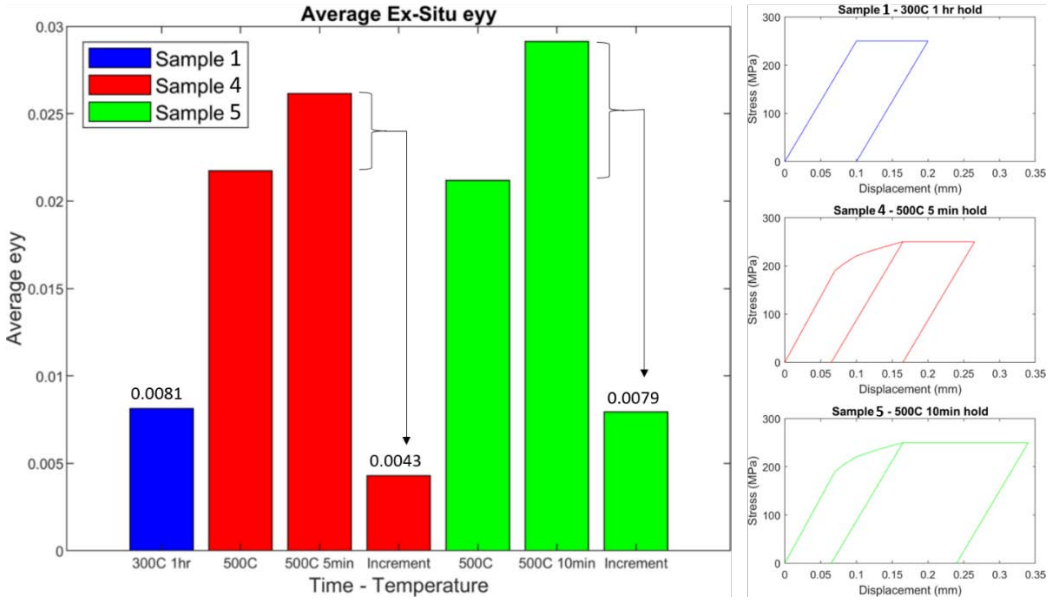

Figure 28: Bar plot of average strains after each loading step for samples #4 and #5, as well as the first step for sample #1. The loading histories of each case are shown on the right.

Finally, in order to evaluate the underlying mechanism driving deformation, a representative volume element (RVE) analysis was conducted on all samples, on all load steps. The idea behind this analysis is to *measure* the RVE's for each of these steps, in an attempt to quantify the non-uniformities present on the strain fields, which should allow us to identify different mechanisms. This analysis follows the procedure described in [14].

An RVE can be understood as the *minimum* box size for which the standard deviation of the distribution of average strains for many boxes covering the entire strain field deviates from being approximately constant. For each box size, 25,000 boxes are taken randomly, and the average strain within each box is calculated. Finally, the standard deviation of the distribution of average box strains for each box size is plotted against box size. The resulting plot for sample #1 is shown in Figure 29. At large box sizes (the right-hand area of the plot in Figure 29, box sizes from 350 to 400 μm) the trailing points of the plot are capable of capturing the average value of the strain field as they are larger than the RVE. We know this since when the stress is averaged in these box sizes, the total average value corresponds to that measured at the far-field. To experimentally estimate the RVE size, which would be the smallest box size capable of capturing the average residual plastic strain response, a straight line is fitted to the standard deviation data in Figure 29 and the region where the points deviate more than 10% from linearity is taken as the RVE size (shown by the arrow in Figure 29). In order to account for the noise seen in Figure 29, the RVE is taken at the first point before 5 succeeding points that go over 10% deviation from linearity.

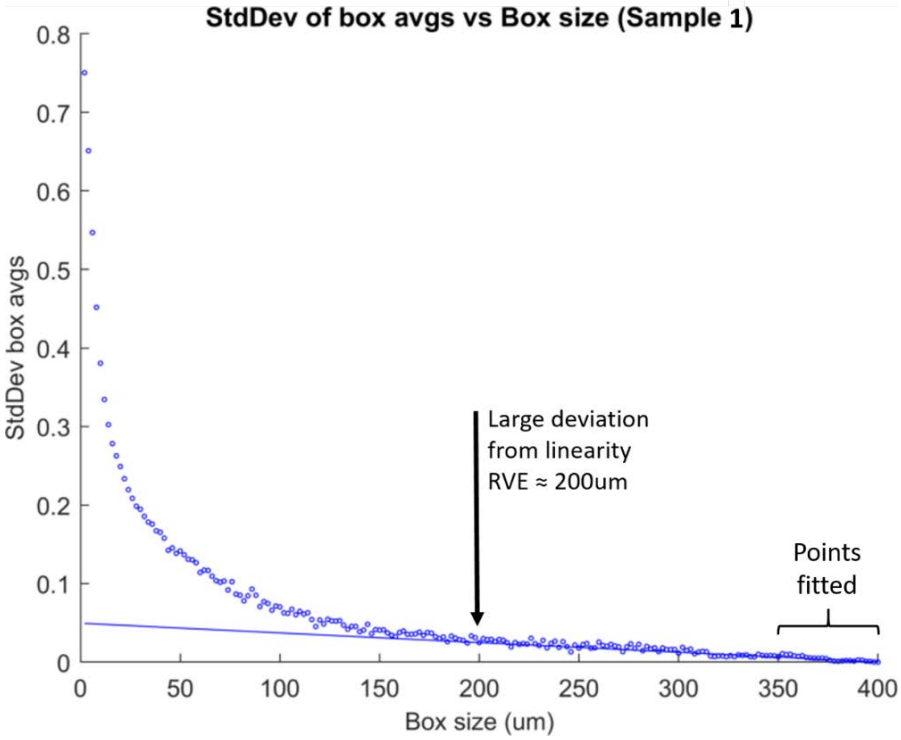

Figure 29: Standard deviation of box strain averages vs. box size for sample #1.

Figure 30 shows the plot for each load step of each sample, color-coded differently for the elastic creep, plastic creep, and purely plastic deformation cycles, in the same axis. The accompanying bar plot shows the RVE sizes for each one of these loading steps, again color-coded for each deformation regimes.

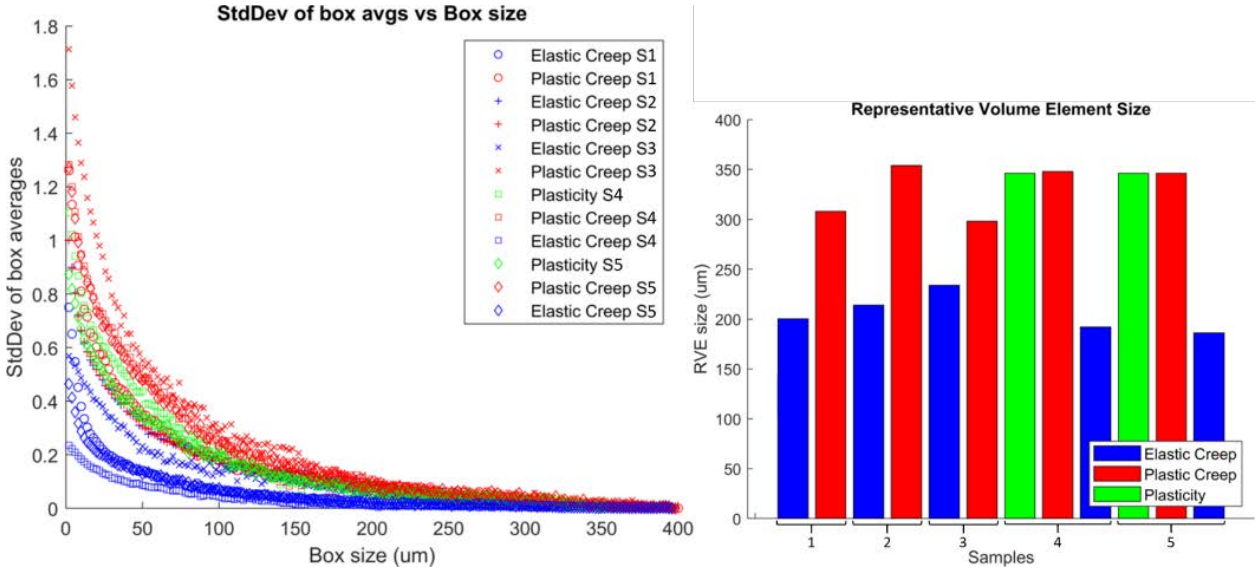

Figure 30: RVE analysis for all samples put together (left) and the results of the corresponding measured RVE sizes (right).

Conclusions: From the obtained results the following conclusions can be drawn:

1) The plastic creep regime is more severe than elastic (pure) creep;

2) Hardening from plastic creep at higher temperatures works to mitigate damage from subsequent elastic creep at lower temperatures;

3) Doubling the elastic creep (at 300°C) time from 1 to 2 hours produced an increase in average strains of 0.15%, while doubling the elastic creep (at 500°C) time from 5 to 10 minutes resulted in a 0.36% increase;

4) The underlying mechanisms, judged from the RVE size for plastic and elastic creep appear to be different. However, since the RVE's for pure plasticity and plastic creep are the same, and also because the results for the elastic creep from samples #4 and #5 (that are an isolation of the elastic creep within a nominally plastic creep regime) fall together with the other elastic creep results, there seem to only truly be two different mechanisms at play: that of creep and that of plasticity, with the latter being the dominant of the two.

9. CREEP-FATIGUE MODELLING

Modeling of creep-fatigue damage accumulation is an open problem in the field of the mechanical behavior of materials. Many models have been proposed [15], but since most are empirically obtained they require considerable experimental data fitting, which makes widespread adoption of these models by industry both cumbersome and costly. Consequently, the most widely used model in terms of design applications consists of adding fatigue and creep damage linearly, as obtained by Miner's rule and Robinson's rule respectively [16], i.e.,

$$\left(\Sigma(^{ni}/_{Ni}) + \Sigma(^{tj}/_{Tj}) = 1\right).$$

It is important to note that the share of the damage caused by fatigue must be calculated from data obtained at the operating temperature, with ni and tj being the number of fatigue cycles and duration of creep "cycles" at given stress range $\Delta\sigma$ (or strain range $\Delta\varepsilon$) and temperature to which the sample was subjected, while Ni and Tj are the number of fatigue cycles and duration of creep "cycles" that would cause failure under the same conditions.

Such a simple rule does not account for any coupling between fatigue and creep damage mechanisms, and because of this, in real life applications empirically determined safety factors need to be applied to account for the expected coupling. For the specific case of austenitic stainless steels that is of interest in

this work, the ASME boiler and pressure vessel code [16], uses an experimentally determined bilinear envelope that restricts safe operation conditions to 0.3 for both fatigue and creep damage (in contrast to the linear rule that would give 0.5 damage for both).

In this section we investigate the applicability of a physics-based model, originally developed by Neu and Sehitoglu [17-18], in predicting creep-fatigue damage accumulation in stainless steel 709. Although the model requires a total of 27 material constants, typically obtained through experimentation, it is shown that many of these constants may be approximated from reference material data. Life predictions from the coupled model for isothermal experiments with and without hold times are shown to be comparable to experimental results.

The model proposed by Neu and Sehitoglu consists of 3 damage equations, one each for the fatigue, oxidation and creep portions of the total damage, as well as a unified constitutive equation employed to compute the relevant stresses needed in each damage equation. The coupling between the three phenomena occurs through the unified constitutive equation. Neu and Sehitoglu [18] describe the experimental data required to determine each one of the material constants present in the model. Our effort follows a scheme outlined in [15] to determine each of these constants from reference data, that is, without the need to obtain specific experimental data for stainless steel 709. The values used for each of the constants are shown in Table 2, along with an explanation of the methodology used for obtaining them.

Three reference materials were used to estimate the value of all constants. Stainless steel 316 is regarded as the commercially available material most closely related to stainless steel 709 [21,22]. 1070 steel was used for some inelastic properties, mainly regarding the shape of the stress strain curve (not the actual values); and Mar-M247, a nickel alloy was used to estimate some oxidation constants, since both materials are expected to form chemically equivalent oxides.

From the list in Table 2, of special interest are: ΔH^{in} and ΔH^{cr} were assumed to be the same, in line with the assumption of the constitutive model that both creep and plasticity are treated as inelastic strains. K, the drag stress, is assumed to be equal to the yield strength. m the creep exponent has a higher than normal value (usually within 1-7) because with cyclic loading the material has to undergo a portion of primary creep every cycle so the exponent is expected to be higher than the ones calculated for the minimum creep rate.

Finally note that of the 23 constants listed in Table 2, only two, D_o and A_{cr}, are fitted to the data that we collected in our experiments. All remaining values were taken from the literature as outlined above.

Table 2: List of material constants used for Neu-Sehitoglu model.

Constant	Description	Value	Obtained
a	Linear thermal expansion Coefficient	$1.86\ 10^{-5}$ mm/mm-°C	Matweb [19] for ss316
E	Young's modulus	194,994 - 73.855*T MPa (T in Celsius)	Nickel development institute [20] for ss316
n_1	Exponent for creep dominated deformation	5.4	Neu-Sehitoglu [18] for 1070 steel
n_2	Exponent for plasticity dominated deformation	8.3	Neu-Sehitoglu [18] for 1070 steel
K	Drag stress	331.7 - 0.2061*T Mpa (T in Celsius)	Swathi et al [21] for ss709
A_o	Scaling constant for inelastic deformation	$5\ 10^9$	Fitted to data
ΔH^{in}	Activation energy for inelastic deformation	277,000 J/mol	Alomari et al. [22] for ss709
σ'_f	Fatigue strength coefficient	738.4 MPa	Non-linear least squares fit to room temperature (RT) fatigue data
b	Fatigue strength exponent	-0.055	
ε'_f	Fatigue ductility coefficient	0.04251	
c	Fatigue ductility exponent	-0.3322	
ξ^{ox}	Oxidation phasing constant	1.3	Calculated from oxidation data from Zamrik et al. [23] for ss316
B	Thermal strain rate sensitivity	0.75	Sehitoglu [24] for Mar-M247 nickel alloy
b	Mechanical stain range exponent	1.5	
D_o	Oxidation scaling constant	$8.68\ 10^5$	Fitted to data
ΔH^{ox}	Activation energy for oxidation	260,722 J/mol	Calculated from oxidation data from Buscail et al. [25] for ss316
H^{cr}	Constant related to critical oxide thickness	$2.4\ 10^{-6}$ m	Neu-Sehitoglu [24] for Mar-M247 nickel alloy
ξ^{cr}	Creep phasing constant	0.5	Neu-Sehitoglu [18] for 1070 steel
ΔH^{cr}	Activation energy for creep	277,000 J/mol	Alomari et al. [22] for ss709
A_{cr}	Creep scaling constant	$5\ 10^{11}$	Fitted to data
m	Creep stress exponent	11.34	Neu-Sehitoglu [18] approximation of phase 1 creep
a_1	Stress state constant	1/3	Assumption of no creep damage under compression
a_2	Hydrostatic stress sensitivity constant	1	

Figure 31 shows the resulting predictions along with the same experimental data. The three curves show, with varying degrees, a transitioning behavior from creep dominated damage at lower strain rates to fatigue dominated damage at higher strain ranges. There is a general agreement with the experimental data for the 650°C case with no hold time (red data and line). Although the numbers are not directly comparable, the apparent transition in dominant mechanism is captured with the knee in the curve (a characteristic lacking from the traditional Coffin-Manson fit). Also, although there are less data in those cases, the model predicts well the measured life for creep-fatigue cases with both a 2 min (green data and line) and 30 min (blue data and line) hold time in each cycle.

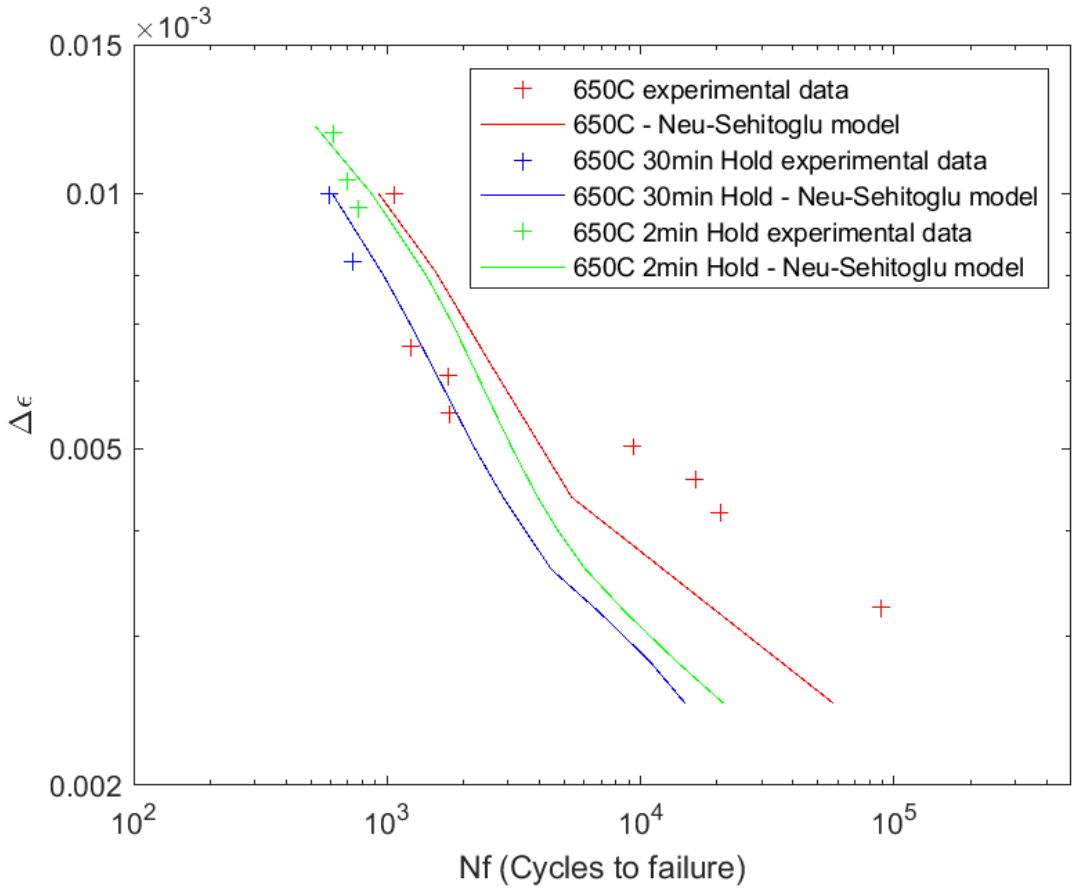

Figure 31: Neu-Sehitoglu model predictions along with experimental data.

Finally, in order to assess the validity of the model and to compare it to the well-established linear model, a plot showing fatigue damage vs creep damage can be constructed, using the data points with hold times. For the linear model, fatigue damage is taken directly from the Coffin-Manson fit of experimental data at 650°C, while creep damage is calculated using creep data obtained from Potirniche [26] and Shaber et al. [27]. It is interesting to note that, because of this, the linear model takes an approach that overestimates

the fatigue damage, since at high temperatures (even without hold times) there is considerable creep damage occurring, in order to compensate for underestimating creep damage, that is calculated considering uniaxial creep instead of cyclic creep (lower creep exponent and hence less deformation). Figure 32 shows a plot of Fatigue damage vs Creep damage, for the same data points shown in Figure 31, calculated using both the linear model and the Neu-Sehitoglu model. Along with the data points, two lines are drawn, showing the assumed limits from the linear model and from the ASME recommended envelope.

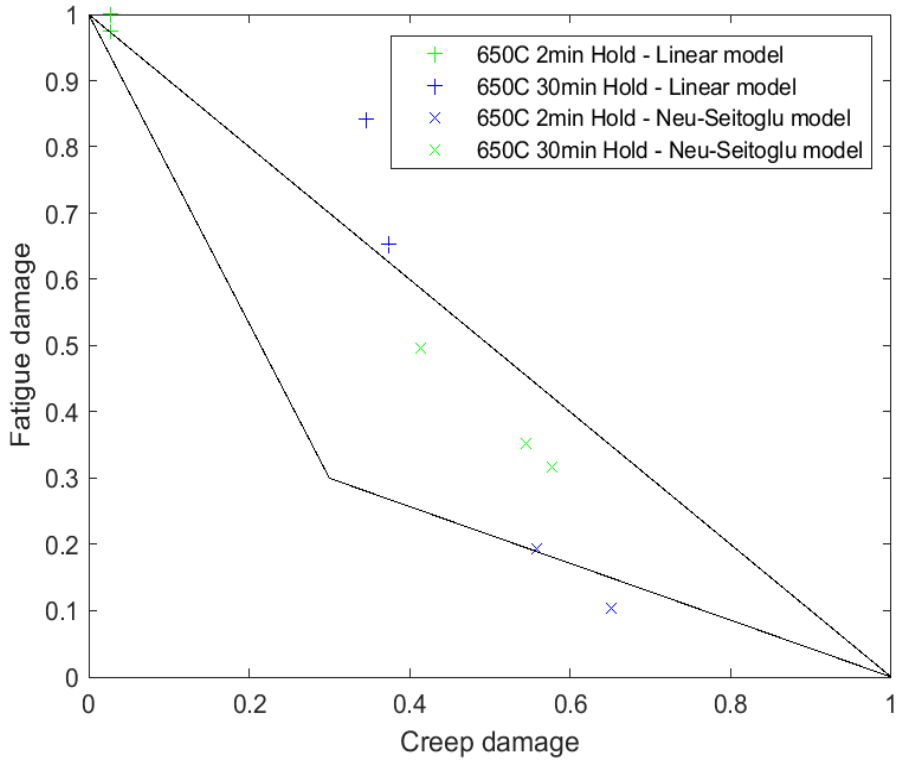

Figure 32: Fatigue vs Creep damage for linear model and Neu-Sehitoglu model.

The results from both models are mostly above the ASME recommended envelope, which is expected, since the ASME code is supposed to give a conservative basis for thermomechanical fatigue design. That being said, the results for the linear model are further away from the envelope, which would indicate a less conservative approach than the Neu-Sehitoglu model. Since for the same data points the results indicate a more critical combination of fatigue and creep damage. One of the points from the Neu-Sehitoglu model did fall below the ASME recommendation, which would indicate that the code might actually be non-conservative for certain conditions. Note that the same code has been found to produce non-conservative results for other materials (namely 1CrMoV steel) by Wiswanathan [28].

Conclusions: The model proposed by Neu and Sehitoglu [18] was shown to produce good life predictions for stainless steel 709 samples loaded at 650°C both with and without hold times. The predicted lives fall well within one order of magnitude of the measured values. Given the results, the estimation of the material constants through the use of reference materials was shown to be valid, and the model could be applied and verified for different loading conditions.

In comparison to the widely accepted linear model, the Neu-Sehitoglu model produced more conservative results, closer to the also well-established ASME code for pressure vessels recommendation. One of the data points obtained from the Neu-Sehitoglu predictions would suggest a non-conservative prediction from the ASME code, which has been shown to be the case for some materials/test conditions in the past.

The modeling of creep-fatigue interactions remains an open problem in the field of thermomechanical behavior of materials, and the unlocking of such complex mechanisms would require a coordinated effort to obtain data similar to what is presented on this report (all of the material constants required for a physics based thermomechanical fatigue model) for many different materials.

10. PUBLICATIONS FROM THIS EFFORT

R.B. Vieira, C.Kim, H. Sehitoglu and J. Lambros, “Microstructural Strain Evolution During Creep-Fatigue of an Austenitic Stainless Steel”, presented at Annual Conference 2017, Society for Experimental Mechanics (SEM).

R.B. Vieira, R. Sidharth, H. Sehitoglu and J. Lambros, “High resolution digital image correlation study of damage accumulation during creep-fatigue of 709 Stainless Steel alloy”, presented at Annual Conference 2018, Society for Experimental Mechanics (SEM).

R.B. Vieira, R. Sidharth, H. Sehitoglu and J. Lambros, “Using High-resolution Digital Image Correlation to Determine Representative Volume Elements in Plasticity and Creep of Metals”, submitted for Annual Conference 2020, Society for Experimental Mechanics (SEM).

11. REFERENCES

[1] Chaboche, J.L., 2008. A review of some plasticity and viscoplasticity constitutive theories. International Journal of Plasticity, Special Issue in Honor of Jean-Louis Chaboche 24, 1642–1693.

[2] Chen, W., Kitamura, T., Feng, M., 2018. Creep and fatigue behavior of 316L stainless steel at room temperature: Experiments and a revisit of a unified viscoplasticity model. International Journal of Fatigue 112, 70–77.

[3] Taleb, L., Cailletaud, G., 2011. Cyclic accumulation of the inelastic strain in the 304L SS under stress control at room temperature: Ratcheting or creep? International Journal of Plasticity, Special Issue In Honor of Nobutada Ohno 27, 1936–1958.

[4] Yu, L., Song, X., You, L., Jiao, Z., Yu, H., 2015. Effect of dwell time on creep-fatigue life of a high-Nb TiAl alloy at 750°C. Scripta Materialia 109, 61–63.

[5] Chen, G., Zhang, Y., Xu, D.K., Lin, Y.C., Chen, X., 2016. Low cycle fatigue and creep-fatigue interaction behavior of nickel-base superalloy GH4169 at elevated temperature of 650°C. Materials Science and Engineering: A 655, 175–182.

[6] Keskin S.B., Sahmaran M., Yaman I.O., Lachemi M., 2014, "Correlation between the viscoelastic properties and cracking potential of engineered cementitious composites." Construction and Building Materials, 71, 375–383

[7] Mehta P.K., Monteiro P.J.M., Concrete; microstructure, properties, and materials. New York, McGraw-Hill, 2006.

[8] Zhang X., Tu S.-T., Xuan F., 2014, "Creep–fatigue endurance of 304 stainless steels." Theoretical and Applied Fracture Mechanics 71, 51–66.

[9] Wareing, J., 1977, "Creep–fatigue interaction in austenitic stainless steels." Metallurgical Transactions A 8, 711–721.

[10] Challenger K.D., Miller A.K., Langdon R.L., 1981, "Elevated temperature fatigue with hold time in a low alloy steel: A predictive correlation." Journal of Materials for Energy Systems 3, 51–61.

[11] Ashby, M.F., "A first report on deformation-mechanism maps." Acta Metallurgica, 1972, v. 20, p. 887.

[12] R.A. Stevens, P.E.J. Flewitt, "The dependence of creep rate on microstructure in a γ′ strengthened Superalloy." Acta Metallurgica, 1981, v. 29 - 5, p. 867.

[13] Kakehi, K. "Effect of primary and secondary precipitates on creep strength of Ni-base superalloy single crystals." Material Science and Engineering, 2000, v. 278, p. 135.

[14] C.Efstathiou, H. Sehitoglu, J. Lambros, "Multiscale strain measurement of plastically deforming polycrystalline titanium: Role of deformation heterogeineities." International Journal of Plasticity, 2010, v. 26, p. 93.

[15] Sehitoglu, H., "Thermo-Mechanical Fatigue Life Prediction Methods," Advances in Fatigue Lifetime Predictive Techniques, ASTM STP 1122, M. R. Mitchell and R. W. Landgraf, Eds., American Society for Testing and Materials, Philadelphia, 1992, pp. 47-76.

[16] ASME boiler and pressure vessel code, American society of mechanical engineers.

[17] Neu, R., and Sehitoglu, H., "Thermo-Mechanical Fatigue, Oxidation and Creep: Part I--Experiments," Metallurgical Transactions, Vol. 20A, 1989, pp. 1755-1767.

[18] Neu, R., and Sehitoglu, H., "Thermo-Mechanical Fatigue, Oxidation and Creep: Part II--Life Prediction," Metallurgical Transactions, Vol. 20A, 1989, pp. 1769-1783.

[19] Matweb.com "AK Steel 316 Austenitic Stainless steel thermal properties"

[20] Nickel development institute, "High-temperature characteristics of stainless steels", A Designers' Handbook series, n 9004.

[21] Swati, U., Li, H., Bowen, P., Rabiei, A., “A study on tensile properties of Alloy 709 at various temperatures”, Material Science and Engineering A, Vol. 733, 2018, pp. 338-349.
[22] Alomari, A.S., Kumar, N., Murty, K.L., “Investigation on Creep Mechanisms of Alloy 709”, Proceedings of the ASME 2017 Nuclear Forum, NUCLRF2017, June 26-30, 2017, Charlotte, North Carolina, USA.
[23] Zamrick, S.Y., Davis, D.C., Firth, L.C., “Isothermal and Thermomechanical Fatigue of Type 316 Stainless Steel”, Thermomechanical fatigue behavior of materials: Second Volume, ASTM STP 1263, M.J. Verrilli and M.G. Castelli, Eds., American Society for Testing and Materials, 1996.
[24] Sehitoglu, H., Boismier, D.A., “Thermo-Mechanical Fatigue of Mar-M247: Part 2—Life Prediction”, J. Eng. Mater. Technol., 1990, Vol. 112(1), pp. 80-89.
[25] Buscail, H., Rolland, R., Perrier, S., “Cyclic oxidation of AISI 316 stainless steel - influence of water vapour between 800 and 1000°C”, Corrosion Engineering, Science and Technology, Vol. 49(3), pp. 169-179.
[26] Potirniche, G., “Characterization of Creep-Fatigue Crack Growth in Alloy 709 and Predictions of Service Lives in Nuclear Reactor Components”, Nuclear Energy University Program Research, Project n15-8623, Final Report, 2019.
[27] N. Shaber, R. Stephens, J. Ramirez, G. P. Potirniche, M. Taylor, I. Charit, H. Pugesek, (2019): Fatigue and creep-fatigue crack growth in alloy 709 at elevated temperatures, Materials at High Temperatures, DOI: 10.1080/09603409.2019.1664079.
[28] Wiswanathan, R., “Damage Mechanisms and Life Assessment of High Temperature Components”, ASM 1995.

U.S. DEPARTMENT OF ENERGY
Nuclear Energy

Multi-scale experimental study of creep-fatigue failure initiation in a 709 Stainless Steel alloy using high resolution digital image correlation

OVERVIEW

Purpose: To understand the multi-scale (micro-, meso-, and macro-scale) development of damage in creep-fatigue of Stainless Steel 709 at high temperatures so that fatigue life modeling predictivity will become feasible.

Objectives: Specifically we wish to address the following questions:
- Is there a quantitative relation between 709 microstructural features (such as grain boundaries and precipitates) and fatigue damage accumulation?
- What factors control (quantitatively) the evolution of distributed damage accumulation into the localization of fatigue crack initiation?
- How does thermal and mechanical cycling affect damage accumulation in 709? For example, do in-phase vs. out-of-phase vs. offset-phase vs. isothermal loading with tensile or compressive hold periods result in different damage content, and if so, how?
- Is there an "additive" effect of creep and fatigue damage? i.e., to what extent are additive damage laws valid in the creep-fatigue of 709, and if they are not valid, are the alternative cumulative damage "laws"?

IMPACT

Logical Path: (i) perform detailed experimental studies of creep-fatigue response over a range of relevant material length scales, temperatures, times, and to the extent possible, different microstructures. Experiments will be based on digital image correlation techniques and will provide strain measurements that are full-field, non-contact, high-resolution and multi-scale;
(ii) incorporate the experimental observations in a predictive modeling framework for the long term creep-fatigue failure prognosis in extreme coupled environments using a physically-based (energy minimization of dislocation slip and dislocation/particle interaction) fatigue damage initiation model.

Outcomes: This work will focus on combined creep and fatigue thermo-mechanical loading, as opposed to only creep. The effort will be primarily experimental and will provide a detailed dataset of full-field strain measurements at both the aggregate grain and the sub-grain levels. As such it will show in detail how damage forms and progresses. A modeling effort will take an existing physically based slip band energy minimization model, and modify it appropriately to incorporate temperature effects.

DETAILS

Principal Investigator: John Lambros

Institution: University of Illinois Urbana-Champaign (UIUC)

Collaborators: H. Sehitoglu (UIUC)

Duration: 4 years

Total Funding Level: $800,000

TPOC: Yanli Wang

Federal Manager: Sue Lesica

Workscope: RC-3.1

PICSNE Workpackage #:
NU-15-IL-UIUC-0601-01P
Project Number: 15-8432

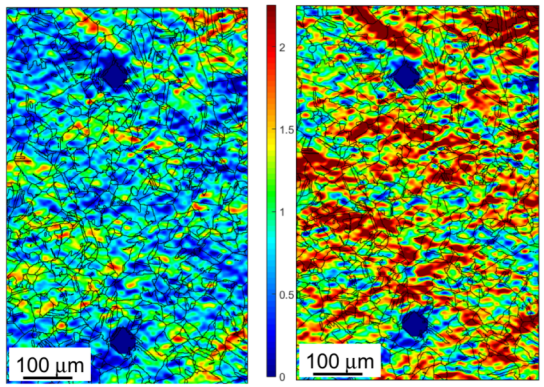

RESULTS

Results: In this project we (a) performed high-resolution digital image correlation measurements (HiDIC) of plasticity in alloy 709 (images on left); (b) quantified damage accumulation at the microstructure under fatigue, TMF, and creep-fatigue conditions of 709; (c) Studied the role of hold times, i.e., adding a creep component, to RT and high temperature fatigue; (d) Studied the mechanisms of thermomechanical fatigue in 709; (e) Investigated the existence of a time-temperature interchangeability criterion to aid in accelerated creep-fatigue testing;
(f) Established the validity of a combined creep-fatigue model for life prediction, namely the Neu-Sehitoglu model for 709 (image right shows the model predictions for various cases).

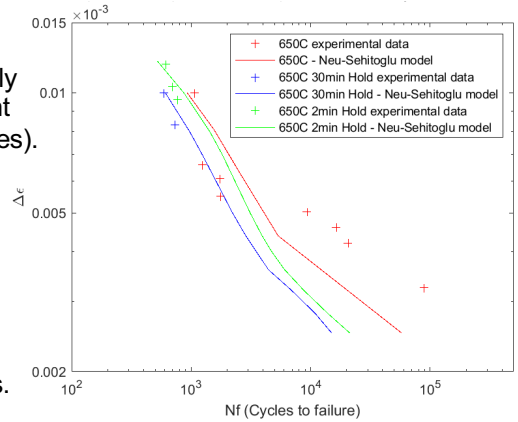

Accomplishments: We have participated in several conferences and have prepared extended abstract for these conferences. We are also in the process of preparing 3 journal paper publications. The project has also had participation of 2 MS, 1 Ph.D. graduate students, and two faculty members.